

GPS METEOROLOGY AND THE PHENOMENOLOGY OF
PRECIPITABLE WATER

A DISSERTATION SUBMITTED TO THE GRADUATE DIVISION OF THE
UNIVERSITY OF HAWAI'I IN PARTIAL FULFILLMENT OF THE
REQUIREMENTS FOR THE DEGREE OF

DOCTOR OF PHILOSOPHY
IN
GEOLOGY AND GEOPHYSICS

DECEMBER 2002

By

James H. Foster

Dissertation Committee:

Michael Bevis, Chairman

Patricia Cooper

Gerard Fryer

Frederick Duennebier

Steven Businger

We certify that we have read this dissertation and that, in our opinion, it is satisfactory in scope and quality as a dissertation for the degree of Doctor of Philosophy in Geology and Geophysics

DISSERTATION COMMITTEE

McBewis

Chairman

George J. Ryan

[Signature]

Bob Cozz

Alvin Busby

Abstract

Three studies of precipitable water using the Global Positioning System are presented. The first study finds that precipitable water in Hawai'i is best described by a lognormal distribution. The long-term average value of precipitable water declines exponentially with height, but the dispersion of precipitable water declines more linearly. The change in skewness of the distributions is also linear, although in this case it increases with elevation. The second and third studies use GPS meteorology to investigate a climatological and a meteorological event respectively. First, the effect of the 1997-1998 El Niño on precipitable water in the western tropical Pacific is studied and found to be consistent with a model relating the formation of an anomalous high-pressure ridge to the El Niño episode. Finally, the details of the precipitable water field for the Ka`ū Storm, November 2000 are examined. The results highlight the role of topography in controlling the location of convection. The observed correlation between the precipitable water and rainfall is used to generate estimates of rainfall based on GPS data. Comparing the GPS precipitable water estimates with those from a weather model indicates that the underestimates of rainfall produced by the weather model are probably due to correlated underestimates of precipitable water.

Table of Contents

Abstract.....	iii
Table of Contents	iv
Table of Figures	vi
Chapter 1: Introduction	1
Chapter 2: Lognormal Distribution of Precipitable Water in Hawai`i	4
Abstract	4
Introduction.....	4
Data and Analysis	5
The Lognormal Distribution	7
Results	9
Discussion and Conclusions	14
Acknowledgments	17
Chapter 3: El Niño, water vapor, and the Global Positioning System	18
Abstract	18
Introduction.....	19
Results	20
Conclusions.....	25
Acknowledgments	26
Chapter 4: The Ka`ū Storm (Nov 2000): Imaging precipitable water using GPS	27
Abstract	27
Introduction.....	29
Network and Data Methodology.....	31
Results	35
Temporal Structure of the Precipitable Water	35
Spatial Structure of the Precipitable Water	37

Precipitable Water and Rainfall	44
GPS and the Mesoscale Spectral Model.....	54
Conclusions	58
Acknowledgements	61
References.....	62

Table of Figures

Figure 2.1. Location of GPS sites on the Big Island of Hawai'i. Sites with colocated meteorological instruments are the solid black circles	6
Figure 2.2. Histograms of precipitable water for MKEA, PGF2, and PGF4 with lognormal PDF curves superimposed. The parameters τ , m , and s for each PDF curve are: -1, 2.19, 0.581; 0, 20.45, 0.301; 0, 28.14, 0.256 respectively.	8
Figure 2.3. Histograms of the three zenith delays for PGF2 with lognormal PDF curves superimposed. The parameters τ , m , and s for each PDF curve are: 2147.5, 2268.1, 0.313; 2000, 2139.5, 0.030; 0, 127.28, 0.304 respectively.	10
Figure 2.4. Plots showing the elevation dependence of the PW population averages and dispersions. a) Mean (triangles) and median (circles) values. Sites with colocated meteorological instruments are shown as solid black. Best fit exponential functions given by $a \exp(-b \text{ elev})$ where $a = 32.15$, $b = .0005911$ and $a = 31.62$, $b = .0006613$ respectively. The PW scale heights implied are ~1700 and ~1500. b) Arithmetic (triangles) and geometric (circles) standard deviations. The arithmetic standard deviation (ASD) has units of mm of PW while the GSD is dimensionless. The GSD has been multiplied by 10 to plot on the same range. The best-fit linear functions are given by $a + b \text{ elev}$ where $a = 7.62$, $b = -0.00137$ and $a = 0.222$, and $b = 0.000111$ respectively. c) Median PW plotted on a log elevation scale. Intersection is at ~544 m.....	11
Figure 2.5. Histograms and lognormal PDF curves for various elevation levels for the RAOBS at Lihue, Kauai. Histograms were generated by interpolating the cumulative PW profiles for launches from 1998 to 2002 to a common set of elevations. Histograms are arbitrarily shifted vertically for clarity. The scale bar indicates the frequency of PW falling within any given 1 mm interval (bar is 1 mm wide). Shown as insets are the distribution medians and geometric standard deviations (GSD) with respect to height.	15

Figure 3.1. Locations of existing IGS CGPS sites in the western tropical Pacific with sea-level pressure and surface winds for (a) November 1997, just prior to the onset of atmospheric drying and (b) January 1998 when the drying episode was fully developed. Sites discussed here have white boxes under their names. (GPS data from the Hawaiian sites KOKB and MKEA show anomalies similar to GUAM. NTUS was installed in 1998 and TAIW has data only until 1997).21

Figure 3.2. a) GPS-derived precipitable water (PW) series for KWJ1. Green dots are PW estimates, the thick black line is the running 30-day median PW value and the gray shading represents the area encompassing 95% of the estimates. Also plotted is outgoing long-wave radiation (OLR), sea-surface temperature (SST) and rainfall time series for the same period. Red arrows show the onset of El Niño conditions indicated by (b). Black arrows indicate the sudden onset of drying. Blue arrows mark the beginning of La Niña. OLR is used as a measure of convection. Deep, strong convection carries clouds higher, cooling the tops and lowering their thermal emittance, thus low OLR values reflect a moist, deeply convecting atmosphere while high values indicate a dry, cloudless and non-convecting atmosphere. (OLR data are linearly interpolated to each site from the 2.5° grid of daily-averaged data measured by AVHRR on NOAA 14). Reduction of ZND to PW used predicted meteorological data from a 3-D global weather model.23

Figure 4.1. Location map showing the GPS sites and rain gauges used in this study. Rain gauges are marked by triangles, GPS sites by circles. The MSM-modeled surface wind field for 0000Z 3rd November (day 308) is overlain in dark gray arrows to illustrate the regional wind field for the storm event.....28

Figure 4.2. a). Five GPS-derived precipitable water time series representing a vertical profile from sea-level at PGF6 to MLSP at 4050 m on the summit of Mauna Loa. Also shown as the lines marked a-d are the four times for which map-views are presented in Figure 3. b)

Rainfall from Kapāpala Ranch, to the west of the GPS transect and site of the highest measured rainfall for this event.	36
Figure 4.3. Map views of precipitable water estimates for the epochs (a-d) marked in Figure 2. a) 04:00 (HST) 1 st Nov, during the precursory drying event. b) 08:00 (HST) 1 st Nov, all sites show a rapid rise in PW. c) 01:00 (HST) 2 nd Nov, as the Hilo and high-level PW peaks, and d) 09:00 (HST) 2 nd Nov, as the low level PW on the south slopes of Kīlauea peaks and Kapāpala Ranch records its maximum rain rates. (Note that the Mauna Kea station went offline sometime after the peak of the storm.).....	39
Figure 4.4. Maps showing the normalized variability of PW (NPW) for the same epochs as Figure 4.3. $NPW = (PW - M_{PW})/GSD_{PW}$. M_{PW} is the long-term median PW value at a site and GSD_{PW} is the long-term geometric standard deviation.....	42
Figure 4.5. Four GPS and rain-gauge site-pairs showing the relationship between the precipitable water and rainfall time-series. (MLSP was used instead of MOKP, which is closer to the rain gauge, because MOKP was not active until after the main storm event had passed.) In addition to the absolute PW, the long-term median PW values and the +1, +2 and +3 standard deviation values are shown. The vertical range for the 4 panels has been chosen to provide the same vertical scaling for the PW.	45
Figure 4.6. Plot of total rainfall for this event against elevation of the gauges. The four gauges chosen in Figure 4.5 for their proximity to GPS sites fall within well-defined group shown with the larger filled circles. This group is chosen to represent the regional relationship with the function: $RAIN = 826 - 0.1952 \times ELEV$	49
Figure 4.7. Scatter plot showing rain rates vs. precipitable water for the four site-pairs in Figure 4.5: MLSP/MOK (diamonds), UWEV/UWEV (circles) WAOP/POC (triangles) and HILO/HILO (squares). The 4 data sets have been displaced vertically for clarity and the vertical (rain rate) scale is shown. The empirically determined bounds to the data are shown as dotted and solid lines. The lower bound (dotted line) is described by the equation	50

Figure 4.8. Map views of the GPS-derived predictions of rainfall. The equation used to map PW into rainfall is given in Figure 4.7.52

Figure 4.9. Bar graphs of accumulated 3-hr rainfall for UTC day 307 for the MSM and GPS estimated rainfall and the measured rainfall. Gauges 1-9. MSM predicted rainfall shown as black bars, GPS-derived estimates in gray and observed values in white.....55

Figure 4.10. See Figure 4.9. Gauges 10-16.56

Figure 4.11. MSM predicted precipitable water and GPS observed precipitable water, indicating pervasive MSM underestimate for higher values.....57

Figure 4.12. Misfit between MSM predicted rainfall and observed rainfall plotted against the misfit between MSM predicted precipitable water and GPS estimated precipitable water. Dashed line indicates median fit to the data with the one extreme outlier removed.59

Chapter 1: Introduction

The importance of the roles that atmospheric water vapor plays in climate and weather systems can hardly be overstated [Anthes, 1983; Starr and Melfi, 1991]. Knowing its distribution in space and time is crucial to better understanding of climate and climate change and weather modeling and forecasting. The vertically integrated water vapor content of the atmosphere, or precipitable water (PW) is also a quantity of great interest to space geodesists. Water vapor induces a delay in radio signals propagating through the atmosphere that is highly variable in space and time. In order to achieve the desired sub-centimeter accuracy using space-based geodetic systems such as the Global Positioning System (GPS), Very Long Baseline Interferometry (VLBI) and Interferometric Synthetic Aperture Radar (InSAR) the PW delay must be accounted for [Hogg et al., 1981; Lichten and Border, 1987; Truehaft and Lanyi, 1987; Tralli et al., 1988].

GPS Meteorology inverts this problem and uses networks of continuously operating GPS stations to estimate the PW history above each station in the network [Bevis et al., 1992; Duan et al., 1996]. The propagation delay of the GPS signal as it travels through the neutral atmosphere has wet and hydrostatic (or 'dry') components. The hydrostatic delay is proportional to the total mass of atmosphere along the radio path, and hence to surface pressure, while the wet delay is nearly proportional to the total amount of water vapor along the radio path. Both delays increase in a predictable fashion as the path's elevation angle decreases, thereby increasing the length of the path within the atmosphere. Geodesists usually parameterize delays in terms of zenith (vertical) path delays. GPS measures the total neutral delay. Given surface pressure at a GPS station, we can compute the zenith hydrostatic delay and subtract this from the zenith neutral delay (ZND), and thus isolate the zenith wet delay which, in turn, can be transformed into an estimate of PW [Bevis et al., 1994].

The technical aspects of GPS Meteorology are now reasonably well understood and refined, however, the details of the processes that control the distribution of water vapor and statistics that best describe them are not so well resolved. The processing of space geodetic data and the retrieval of precipitable water estimates from the data could be improved by incorporating the best possible statistical description of water vapor. The first study in this dissertation addresses the weakness in our understanding of the statistics by using 4-year time series of precipitable water from a GPS network in Hawai`i to examine the long-term statistical properties of water vapor. It is found that the lognormal distribution is the best description for precipitable water in Hawai`i which accords well with many previous observations of the lognormal distribution for other meteorological parameters and is also supported by a theoretical derivation for the distribution of relative humidity. The long-term average value of precipitable water declines exponentially with height, but the dispersion of precipitable water declines more linearly. The change in skewness of the distributions is also linear, although in this case it increases with elevation.

Although GPS meteorology is now well established as a reliable tool capable of generating estimates of PW that are sufficiently accurate for both weather and climate studies, the implementation of GPS as an operational meteorological instrument is ongoing. In chapters 3 and 4 GPS Meteorology is used for two case studies. In chapter 3, GPS stations in the western tropical Pacific are used to investigate the effect of the 1997-1998 El Niño on PW. The pattern of sudden drying observed at both stations is found to be consistent with the formation of an anomalous high-pressure ridge connected to the El Niño episode.

In Chapter 4, the Ka`ū Storm, an extreme rain event that impacted the southern and eastern portions of the Big Island of Hawai`i during the 1st and 2nd of November, 2000, is investigated. The temporal and spatial distribution of PW is examined using a network of

GPS receivers and rain gauges and the connection between rainfall and PW is explored. A heuristic algorithm is presented as a potential tool for mapping PW to rainfall. The performance of a local weather model is also examined and its rainfall prediction is found to be limited by its ability to model PW.

Chapter 2: Lognormal Distribution of Precipitable Water in Hawai`i

Abstract

We use four-year time series of precipitable water derived from a GPS network to show that precipitable water in Hawai`i closely approximates a lognormal distribution. The long-term average value of precipitable water declines exponentially with height, but the dispersion of precipitable water declines more linearly. The change in skewness of the distributions is also linear, although in this case it increases with elevation.

Introduction

The importance of the roles that atmospheric water vapor plays in the climate and weather systems can hardly be overstated [Starr and Melfi, 1991; Anthes, 1983]. The vertically integrated water vapor content of the atmosphere, or precipitable water (PW), is also of great interest to space geodesists. Atmospheric water vapor induces a propagation delay in the radio signals from the satellites of the Global Positioning System (GPS) that is highly variable both in space and in time. The statistical properties of PW and the associated 'wet delay' are relevant to geodesists designing algorithms to estimate atmospheric propagation delays from the data collected by networks of geodetic GPS receivers and by related space-geodetic systems such as Very Long Baseline Interferometry [Hogg et al.,

1981; Truehaft and Lanyi, 1987; Lichten and Border, 1987]. With the advent of 'GPS meteorology' where networks of continuously operating GPS stations are used to estimate the PW history above each station in the network [Bevis et al., 1992; Duan et al., 1996; Gutman and Benjamin, 2001] long time series of PW measurements are now becoming available, and this is contributing to a resurgence of interest in the statistics of PW. Most of this research has focused on the autocorrelation structure and power spectra of PW time series acquired at a given point in space, or on the spatial correlation or cross power spectra of PW time series collected at different locations [e.g. Williams et al., 1998; Davis, 2001]. In this paper we take a different approach, and investigate the statistical distribution of PW measurements accumulated over time periods of several years. This initial study is focused on Hawaii because the availability of GPS stations over a wide range of elevations provides us with an unusual opportunity to examine how the statistical distribution of PW varies with height.

Data and Analysis

The GPS network on the Big Island of Hawai'i (Figure 2.1) consists of 24 sites spanning a height range from sea level to the summits of the two main volcanoes, Mauna Kea and Mauna Loa, at ~4000 m. Of these sites only 9 have colocated meteorological instruments to provide direct measurements of pressure and temperature. For these sites the PW is estimated to be accurate to ~1.5 mm [Tregoning et al., 1998]. In order to be able to incorporate the other sites into our study we extrapolated the pressure and temperature fields to each location, constraining the process by incorporating data interpolated from the NCEP Global Reanalyses. The predicted pressures and temperatures have rms errors of ~0.25 mbar and ~1.5 °C respectively. This is sufficiently accurate to permit us to include in our analysis PW solutions from all the sites, with the accuracy for those sites using the extrapolated meteorological data estimated as better than 2 mm.

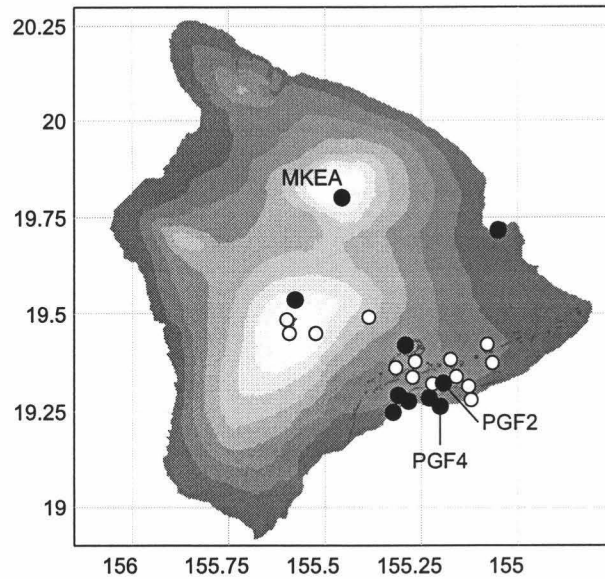


Figure 2.1. Location of GPS sites on the Big Island of Hawai`i. Sites with colocated meteorological instruments are the solid black circles

All GPS data available from 1997 through 2000 were processed using GAMIT [King and Bock, 2000], with 24 atmospheric delay parameters estimated in each 24-hour batch solution (following Duan et al. [1996]), giving hourly estimates of zenith neutral delay (ZND) for the entire 4-year period. Surface pressure was converted to zenith hydrostatic delay (ZHD) [Saastamoinen, 1972] and the mapping parameter Π was calculated from surface temperature using the seasonal climatology determined by Ross and Rosenfeld [1997]. The final transformation into PW is simply given by $PW = \Pi (ZND - ZHD)$.

The Lognormal Distribution

The two most common probability distributions for atmospheric variables are the normal (N) and lognormal (Λ) distributions. Largely through historical chance N became "normal" while the closely related Λ was considered derivative. Stated simply, a variable is considered to be lognormally distributed if its logarithm is normally distributed. For detailed discussion of Λ see Aitchison and Brown [1957]; here we will simply summarize some of the key details.

Whereas the probability distribution function (PDF) for variate X ($-\infty < x < \infty$) is defined by the mean (μ) and the arithmetic standard deviation (σ) if it is distributed according to N, if X is distributed as Λ the PDF is defined in terms of the geometric standard deviation s and the geometric mean or median M , or in terms of s and $m = \log M$ with $0 < x < \infty$. The PDF for X is then given by:

$$\frac{1}{xs\sqrt{2\pi}} \exp\left\{-\frac{(\log x - m)^2}{2s^2}\right\}, 0 < x < \infty$$

The population mean is $M \exp(s^2/2)$ and the population variance is

$M^2 \exp(s^2)(\exp(s^2) - 1)$. Note that the mean is a function of s indicating that a change in the variance of the distribution will also induce a change in the mean. This is an important property with consequences for the interpretation of trends in mean water vapor.

A slightly more general version of Λ is called the 3-parameter distribution. Here an extra term τ is included as a "threshold" parameter. The threshold parameter allows the distribution to

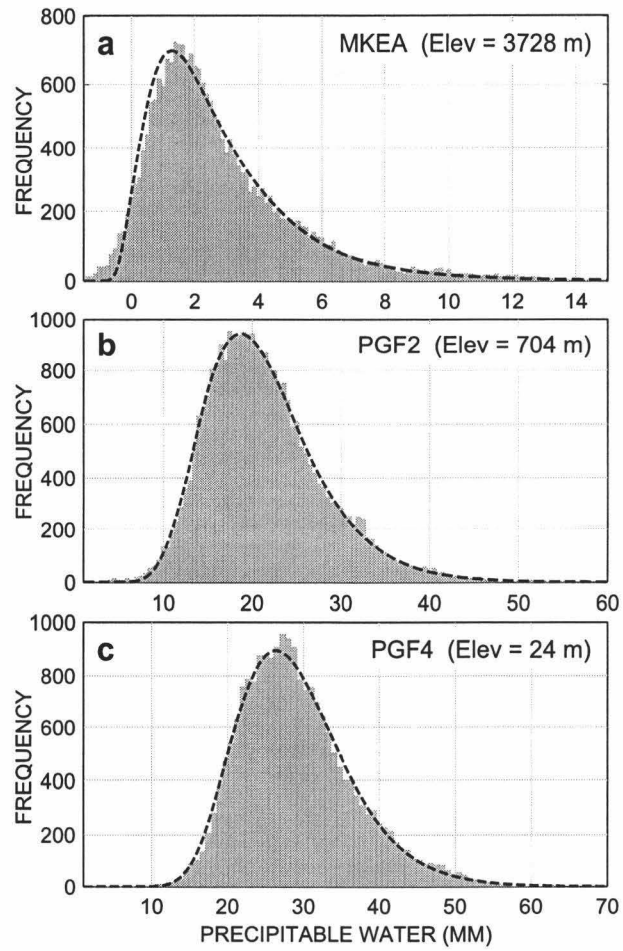


Figure 2.2. Histograms of precipitable water for MKEA, PGF2, and PGF4 with lognormal PDF curves superimposed. The parameters τ , m , and s for each PDF curve are: -1, 2.19, 0.581; 0, 20.45, 0.301; 0, 28.14, 0.256 respectively.

describe the situation where the variable is bounded by some value other than zero and acts to shift the frequency curve. The PDF for the 3-parameter distribution is given by the equation above substituting the variate with $x' = x - \tau$. The 2-parameter form is now the special case where $\tau = 0$. The PDF is now defined for $0 < x - \tau < \infty$ and the locations of the median and mean are shifted by τ while s remains unchanged.

Results

Histograms of PW for three of the sites with colocated meteorological instruments are shown in Figure 2.2 with the derived Λ curves superimposed. PGF4 is near sea level, PGF2 at mid-elevation and MKEA is near the summit of Mauna Kea. These three sites are typical of all results (though the sites without direct meteorological observations are slightly noisier) and show the progression toward more strongly peaked and skewed distributions with increasing elevation. The typical Λ shape is evident for each site with the histogram rising steeply from a threshold value to the peak and with a long tail for the upper portion.

We have extended our analysis to consider the distribution of the ZND measured by GPS, the ZHD computed from surface pressure, and the ZWD ($= \text{ZND} - \text{ZHD}$). The results obtained at PGF2 (Figure 2.3) are characteristic of the entire network. Not surprisingly the ZWD has the form of Λ . In contrast, the ZHD, like pressure, looks more like N. Although the ZHD is always much larger than the ZWD, the ZWD is far more variable in most parts of the world, including Hawai'i, and as a result the ZND has a Λ distribution, or very nearly so.

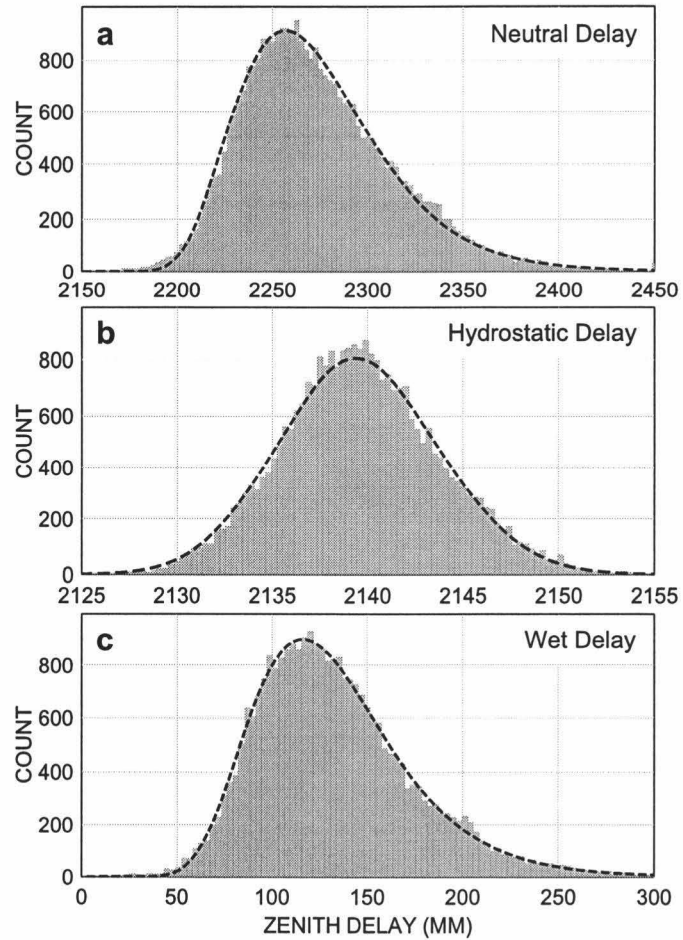
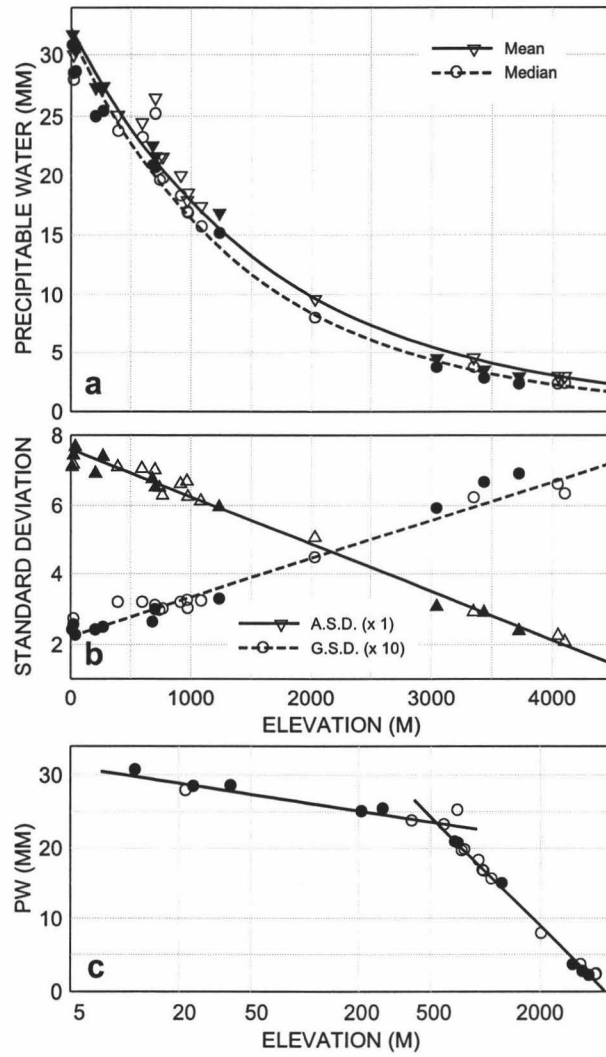


Figure 2.3. Histograms of the three zenith delays for PGF2 with lognormal PDF curves superimposed. The parameters τ , m , and s for each PDF curve are: 2147.5, 2268.1, 0.313; 2000, 2139.5, 0.030; 0, 127.28, 0.304 respectively.

Figure 2.4. Plots showing the elevation dependence of the PW population averages and dispersions. a) Mean (triangles) and median (circles) values. Sites with colocated meteorological instruments are shown as solid black. Best fit exponential functions given by $a \exp(-b \text{ elev})$ where $a = 32.15$, $b = .0005911$ and $a = 31.62$, $b = .0006613$ respectively. The PW scale heights implied are ~ 1700 and ~ 1500 . b) Arithmetic (triangles) and geometric (circles) standard deviations. The arithmetic standard deviation (ASD) has units of mm of PW while the GSD is dimensionless. The GSD has been multiplied by 10 to plot on the same range. The best-fit linear functions are given by $a + b \text{ elev}$ where $a = 7.62$, $b = -0.00137$ and $a = 0.222$, and $b = 0.000111$ respectively. c) Median PW plotted on a log elevation scale. Intersection is at ~ 544 m.



We now turn our attention to the elevation dependence of the PW. In figure 2.4a we plot both mean and median PW against station height. Both mean and median follow the expected exponential form, with PW scale heights of ~1500 m to ~1700 m respectively. These heights need not correspond physically to any real atmospheric layer, but do in fact fall within the normal lower range for the inversion layer in Hawai'i. As we would expect, the mean values are consistently higher than the medians due to the positive skew of the distribution. While the exponential form of the average PW with height is expected, it is perhaps more surprising to see that measures of dispersion of the PW, plotted in 2.4b as both the arithmetic standard deviation (ASD) and geometric standard deviation (GSD), are apparently linear with elevation. While the ASD declines with elevation indicating that the overall range of the PW is decreasing, the GSD shows a linear increase indicating that the skewness of the distribution is increasing with elevation. Plotting the median PW on a log elevation scale to highlight the lower elevation data (Figure 2.4c) reveals that there is a well-defined change in character at ~540 m. This probably represents the mixed layer: the turbulent, statically unstable layer directly affected by surface heating.

Histograms of PW from the National Weather Service radiosonde site in Lihue (Figure 2.5) offer us the opportunity to confirm our observations with an independent data set. The distributions show the same progression from only slightly skewed from N at the surface toward increasing asymmetry with elevation. Like the GPS results, the medians follow an approximately exponential form, however the change at ~540 m is not evident. Instead, like the GSD, these profiles show an inflection between ~1000 and ~3000 m.

Discussion and Conclusions

The lognormal distribution, Λ , appears frequently in meteorology and atmospheric science. Cloud populations [López, 1977], precipitation [Biondini, 1976] and aerosol optical depth [O'Neill et al., 2000] are all distributed lognormally. We have shown that over long periods of time, PW also has a Λ distribution in Hawai'i. Raymond [2000] finds a solution to the moisture transport equations indicating that the relative humidity field tends toward a lognormal distribution providing the temperature and pressure fields are sampled from populations having the same expected value and variance, and that a complex integral function of these parameters tends toward a normal distribution. PW is clearly strongly connected to relative humidity, and as an island environment, Hawai'i is likely to satisfy the former condition. The fact that we do observe a lognormal form for PW suggests that the second condition is also met.

Precipitable water is typically reported using the arithmetic mean and standard deviation, which are closely associated with the normal distribution (see for example Ross and Rosenfeld [1996]) and is often modeled, for example in GPS processing, with an underlying assumption that the stochastic process is sampling a normal distribution. For some cases this might not lead to any serious consequences: the distribution for PGF4 for example, while being clearly lognormal, is not far skewed from normal and so the arithmetic mean and standard deviation may reasonably describe the distribution. For the higher elevation sites however, as the skewness becomes more and more pronounced, it becomes more important to use the more appropriate statistics.

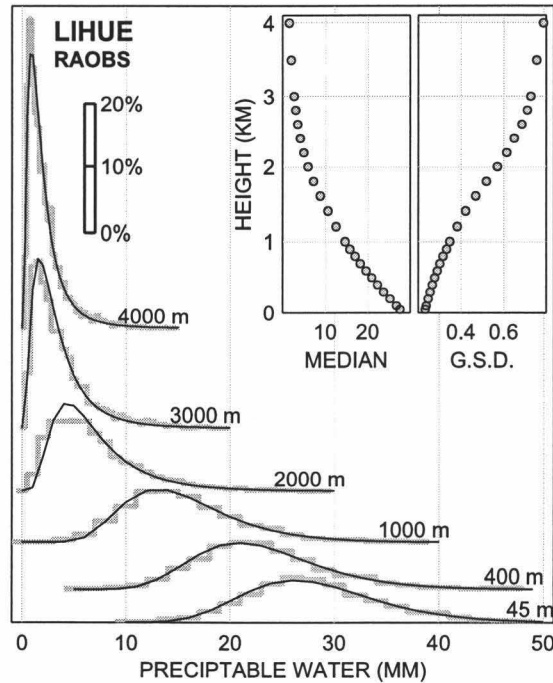


Figure 2.5. Histograms and lognormal PDF curves for various elevation levels for the RAOBS at Lihue, Kauai. Histograms were generated by interpolating the cumulative PW profiles for launches from 1998 to 2002 to a common set of elevations. Histograms are arbitrarily shifted vertically for clarity. The scale bar indicates the frequency of PW falling within any given 1 mm interval (bar is 1 mm wide). Shown as insets are the distribution medians and geometric standard deviations (GSD) with respect to height.

For MKEA (and the other extremely high elevation sites not shown), the Λ PDF fits a little less well than for the lower sites. This is due, at least in part, to the PW estimates drifting slightly negative. These estimates are obviously incorrect, and may be caused by any combination of a number of possible sources: a pressure bias, a small error in the pressure to hydrostatic delay conversion, problems with the mapping function used to calculate the equivalent zenith delay for each satellite elevation angle. Because PW is low for high elevation sites, the impact of any of these biases is magnified. We used a threshold value of -1 in order to get a reasonable fit for the derived PDF for this site and others at similar elevations. Although one interpretation of this value is as a bias for the entire series, we consider it more likely that the median is not significantly biased, but rather that the effects suggested above are skewing the very dry estimates. The observation that the fit is poorest for that section of the histogram close to, and less than, zero seems to support this interpretation. For the lower sites PGF2 and PGF4, no threshold value was needed (i.e. $\tau = 0$) in order to generate the curves shown even though the distributions themselves tend to zero at ~5 mm and ~10 mm respectively. This is aesthetically pleasing, as it seems intuitive that zero, rather than some higher value should be the lower bound for PW in all cases.

The RAOBS data from Lihue are well matched by a family of Λ distributions. The least well modeled histogram is at 2000 m, probably reflecting the influence of the inversion layer. The absence of the abrupt change at ~540 m in the median and GSD profiles is probably a consequence of interpolating the irregularly reported levels to the common set of elevations.

We suggest that it is appropriate to use the median (geometric mean) and geometric standard-deviation that are the natural parameters for the lognormal distribution when

reporting and comparing PW. Although the differences between these parameters and the more commonly reported arithmetic mean and standard deviation may be relatively small, there is a risk, due to the correlation between the arithmetic mean and standard-deviation in a lognormally distributed variable, that using the wrong statistics may lead to errors in interpretation.

We have shown that precipitable water in Hawai'i is best described by a lognormal probability distribution. We are currently studying multiyear PW time series in other parts of the world. While the Λ distribution is not a global property of PW, we do observe it in many places worldwide.

Acknowledgments

We thank Stanford/HVO-USGS for access to data from their GPS sites. The National Park Service Air Resources Division provided some of the surface meteorological data used and the NCEP Reanalysis data was provided by the NOAA-CIRES Climate Diagnostics Center, Boulder, Colorado, from their Web site at <http://www.cdc.noaa.gov/>.

Chapter 3: El Niño, water vapor, and the Global Positioning System

James Foster, Michael Bevis, Thomas Schroeder, Mark Merrifield, Steven Businger, and
Susanne Dorn

SOEST, University of Hawai`ii, Honolulu, HI 96822, USA

Steven Marcus, Jean Dickey, and Yoaz Bar-Sever

Jet Propulsion Laboratory, Pasadena, CA 91109

Published in Geophysical Research Letters, Vol. 27, No. 17, p. 2697-2700, 2000

Abstract

The 1997-1998 El Niño had a profound impact on atmospheric circulation in the tropical Pacific and affected weather patterns worldwide. Precipitable water estimates from Global Positioning System (GPS) sites in the western tropical Pacific capture the sudden onset of large-scale subsidence, a phenomenon proposed as a possible mechanism driving the eventual decline of El Niño episodes. The atmospheric drying associated with this anomalous high-pressure ridge and the turnabout as the warm episode transitions into the subsequent La Niña is clearly visible in the GPS observations.

Introduction

The importance of water vapor in the climate system can hardly be overstated, and knowing its distribution in space and in time is crucial to a better understanding of climate and climate change [Starr and Melfi, 1992]. Networks of continuous Global Positioning System (or CGPS) stations can be used to measure the radio propagation delay associated with the atmosphere, and thus the precipitable water (PW), i.e. total-column integrated water vapor, overlying each GPS station in the network [Bevis et al., 1992; Duan et al., 1996]. While considerable attention has been focused on using this capability to support operational weather analysis and prediction [Businger et al., 1996; Wolfe and Gutman, 2000], much less emphasis has been placed on the climatological uses of ground-based GPS networks. We illustrate this latter class of applications by presenting GPS measurements that manifest atmospheric changes associated with the 1997 - 1998 El Niño event.

The propagation delay of the GPS signal as it travels through the neutral atmosphere has wet and hydrostatic (or 'dry') components. The hydrostatic delay is proportional to the total mass of atmosphere along the radio path, and hence to surface pressure, while the wet delay is nearly proportional to the total amount of water vapor along the radio path. Both delays increase in a predictable fashion as the path's elevation angle decreases, thereby increasing the length of the path within the atmosphere. Geodesists usually parameterize delays in terms of zenith (vertical) path delays. GPS measures the total neutral delay. Given surface pressure at a GPS station, we can compute the zenith hydrostatic delay and subtract this from the zenith neutral delay (ZND), and thus isolate the zenith wet delay which, in turn, can be transformed into an estimate of PW [Bevis et al., 1994].

Results

Two CGPS sites located on islands in the western tropical Pacific (Figure 3.1) recorded the influence of the 1997-1998 El Niño on precipitable water. KWJ1 (Kwajalein) and GUAM (Guam) are located to the northwest of the western Pacific warm pool. KWJ1 sits in the zone where winds from both hemispheres normally converge resulting in a wet climate with relatively little annual variation. Prior to the 1997-1998 El Niño the PW time series for KWJ1 (Figure 3.2a) exhibits little seasonality. There is no clear influence of the El Niño, which began in May 1997 (Figure 3.2b), on PW through most of 1997, however the onset of drying associated with the formation of the pressure ridge and atmospheric subsidence is dramatic. Beginning in November 1997 the GPS observations show a precipitous fall in PW that reached a low from January through March 1998. The PW drop coincided with the out-going long-wave radiation (OLR) increase and the drop in sea-surface temperature (SST) as colder, drier air from higher latitudes cooled the sea-surface. This pressure ridge, much more pronounced during this event than a similar feature that forms in non-El Niño years, may be linked to the anomalous anticyclone identified by Wang et al., [2000]. The formation of this anticyclone during the boreal winter is attributed to a combination of local cooling and remote forcing from the El Niño-related central Pacific warming. Its persistence is postulated as a possible mechanism for the reversal of the El Niño warming trend, as its easterly winds at the equator force upwelling (cold) Kelvin waves to propagate into the eastern Pacific [Wang et al., 2000].

Further north and west, GUAM shows a much stronger annual cycle than KWJ1 with PW, SST, OLR and rainfall all clearly correlated with the East Asian monsoons (Figure 3.2c). The monsoons are seasonal weather patterns driven by the pressure differences caused by

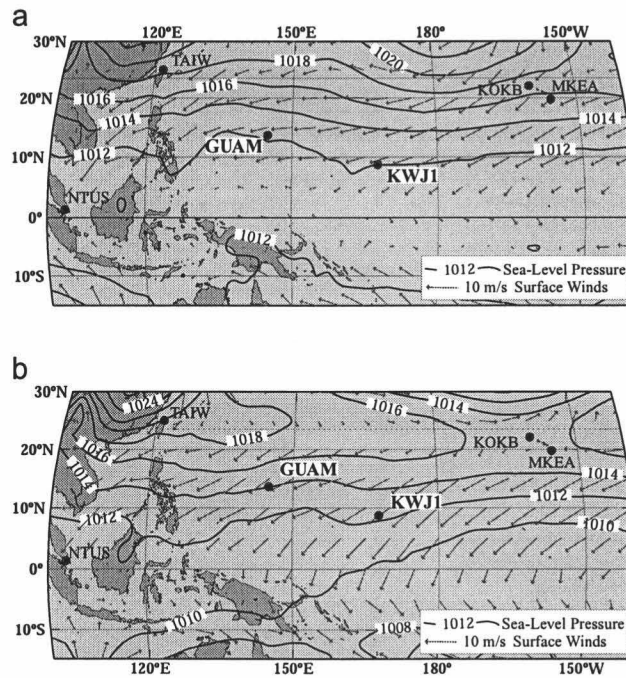


Figure 3.1. Locations of existing IGS CGPS sites in the western tropical Pacific with sea-level pressure and surface winds for (a) November 1997, just prior to the onset of atmospheric drying and (b) January 1998 when the drying episode was fully developed. Sites discussed here have white boxes under their names. (GPS data from the Hawaiian sites KOKB and MKEA show anomalies similar to GUAM. NTUS was installed in 1998 and TAIW has data only until 1997).

the different heat capacities of the continents and the oceans. These pressure differences induce regional wind fields that flow towards the continent during summer and away from it during winter, creating an annual cycle at GUAM with high rainfall during summer/fall and dryer conditions during winter/spring. Because the drop in PW occurred during GUAM's dry season it is somewhat masked and less dramatic, however there is a clear, sudden reduction, starting slightly later than at KWJ1. Although the relative magnitude of the drop was smaller at GUAM, the PW fell to a minimum value similar to that observed at KWJ1 and the OLR and rainfall data both exhibit strong coincident changes. In this case the PW anomaly is uncorrelated with any SST anomaly. This unusually pronounced dry season is consistent with the El Niño-related regional-scale anticyclone modeled by Wang et al. [2000] which is triggered by the winter tradewinds that cause GUAM's normal dry season and then acts to enhance them.

Of particular note for GUAM and KWJ1 is that while both have a normal seasonal drop in median PW during the winter, the variability of their PW estimates (shown by the width of the gray areas in Figures 3.2a and 3.2c) usually increases during this period. The El Niño-induced drop in median value, however, was accompanied by a substantial reduction in the PW variability, reflecting the consistent influence of the subsidence.

GUAM recovered slowly to normal PW levels by summer 1998, and, although KWJ1 remained dry longer than GUAM, it recovered more quickly and also returned to normal values by summer as the high-pressure ridge weakened and the central Pacific warm water anomaly cooled (Figure 3.2b). In both cases the PW begins to recover sooner than the OLR and normal rainfall does not resume until PW reaches near-normal levels.

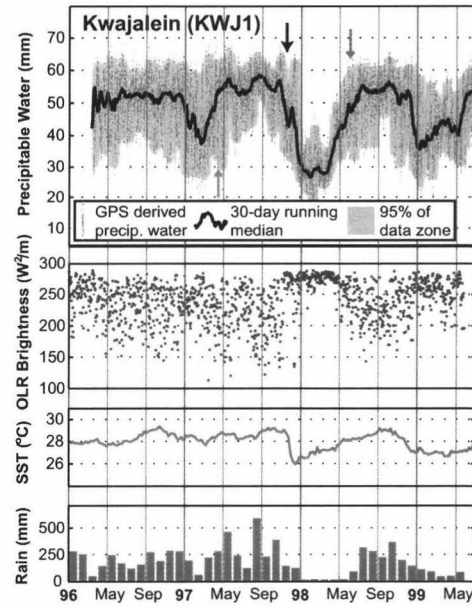
The following year (1998) KWJ1 shows a longer than normal dry season, extending into the spring of 1999 as the subsequent La Niña episode impacted the region. Interestingly

Figure 3.2. a) GPS-derived precipitable water (PW) series for KWJ1. Green dots are PW estimates, the thick black line is the running 30-day median PW value and the gray shading represents the area encompassing 95% of the estimates. Also plotted is outgoing long-wave radiation (OLR), sea-surface temperature (SST) and rainfall time series for the same period. Red arrows show the onset of El Niño conditions indicated by (b). Black arrows indicate the sudden onset of drying. Blue arrows mark the beginning of La Niña. OLR is used as a measure of convection. Deep, strong convection carries clouds higher, cooling the tops and lowering their thermal emittance, thus low OLR values reflect a moist, deeply convecting atmosphere while high values indicate a dry, cloudless and non-convecting atmosphere. (OLR data are linearly interpolated to each site from the 2.5° grid of daily-averaged data measured by AVHRR on NOAA 14). Reduction of ZND to PW used predicted meteorological data from a 3-D global weather model.

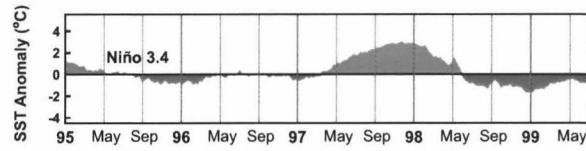
b) Niño 3.4 Index. Niño 3.4 is an indicator for El Niño/La Niña conditions. It is the sea-surface temperature anomaly averaged over the area 5°N – 5°S, 120° – 170°W.

c) GPS derived precipitable water (PW) and other time series for GUAM. Details as for (a).

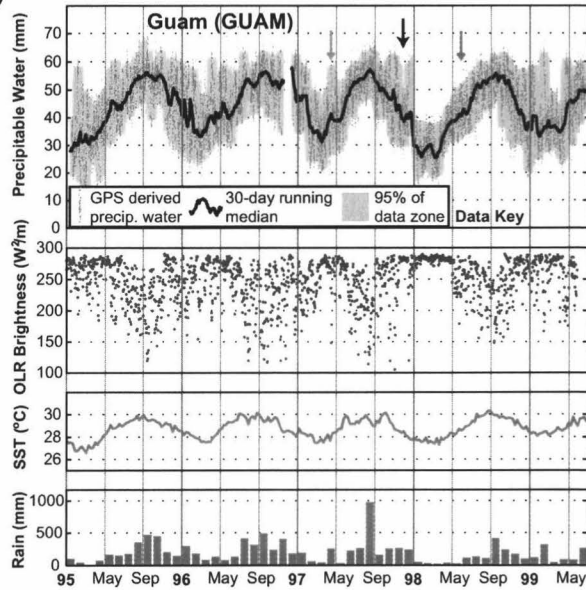
a)



b)



c)



this La Niña did not lead to increased rainfall but instead the drought experienced by these islands was compounded as the center of deep convective activity moved westward during January 1999, away from KWJ1, drying the atmosphere, and stronger surface winds cooled the water. GUAM, in contrast, was now closer to the locus of atmospheric convection so the PW did not drop as low as previous years and the SST remained warmer than normal through this period. The most recent data available for both sites at the time of writing suggest that PW levels had returned to normal values by the end of the spring 1999.

Conclusions

GPS-derived PW estimates from two west Pacific sites capture the impact of El Niño-driven atmospheric changes on PW. During the mature phase of El Niño, an anomalous, high-pressure ridge over the West Pacific resulted in a sharp drop in PW and rainfall over the sites. This anomalous ridge has also been linked to ENSO turnabout. These results illustrate the potential contribution of GPS to climatological investigations. GPS is an accurate, all-weather system, and its high temporal resolution, inherently drift-free nature, and independence from external calibration requirements make it a powerful tool for climate research. The global, and rapidly densifying, International GPS Service (IGS) network provides the framework for both global and regional scale studies.

Acknowledgments

We thank Dr. Bin Wang for useful discussions and Seth Gutman and an anonymous reviewer for their comments. GPS data are from the IGS combined tropospheric solutions where available, augmented with data from JPL and the Pacific GPS Facility. Interpolated OLR data provided by the NOAA-CIRES Climate Diagnostics Center, Boulder, Colorado, from their web site at <http://www.cdc.noaa.gov>. SST data are from the National Meteorological Data Center. Ray Tanabe provided rainfall data. El Niño indices are from the NOAA Climate Prediction Center.

Chapter 4: The Ka`ū Storm (Nov 2000): Imaging precipitable water using GPS

James Foster, Michael Bevis, Yi-Leng Chen, Steven Businger, Yongxin Zhang

SOEST, University of Hawaii

Abstract

We use a network of GPS receivers on the Big Island of Hawai`i to examine in detail the precipitable water field of the Ka`ū Storm, which generated record rainfall and flash floods over much of the southern and eastern portions of the island. With GPS stations distributed from sea level to the highest points on the island, the spatial and temporal variations in precipitable water are investigated as the storm passed over the network. The results highlight the role of the topography in controlling the location of convection, revealing relatively static zones of high precipitable water where onshore winds and terrain anchor the storm. Using the observed correlation between the precipitable water and rainfall estimates of rainfall based on the GPS data are generated. These estimates compare well with most of the high-rainfall sites, but tend to overestimate rainfall for the low rainfall areas. Rainfall predictions from a Mesoscale Spectral Model of the storm consistently underestimate the observed heavy values. Comparison with the GPS, however, suggests that this underestimate is probably due to a correlated underestimate of precipitable water, indicating that significant improvements in predictions could be expected if the precipitable water field can be better constrained.

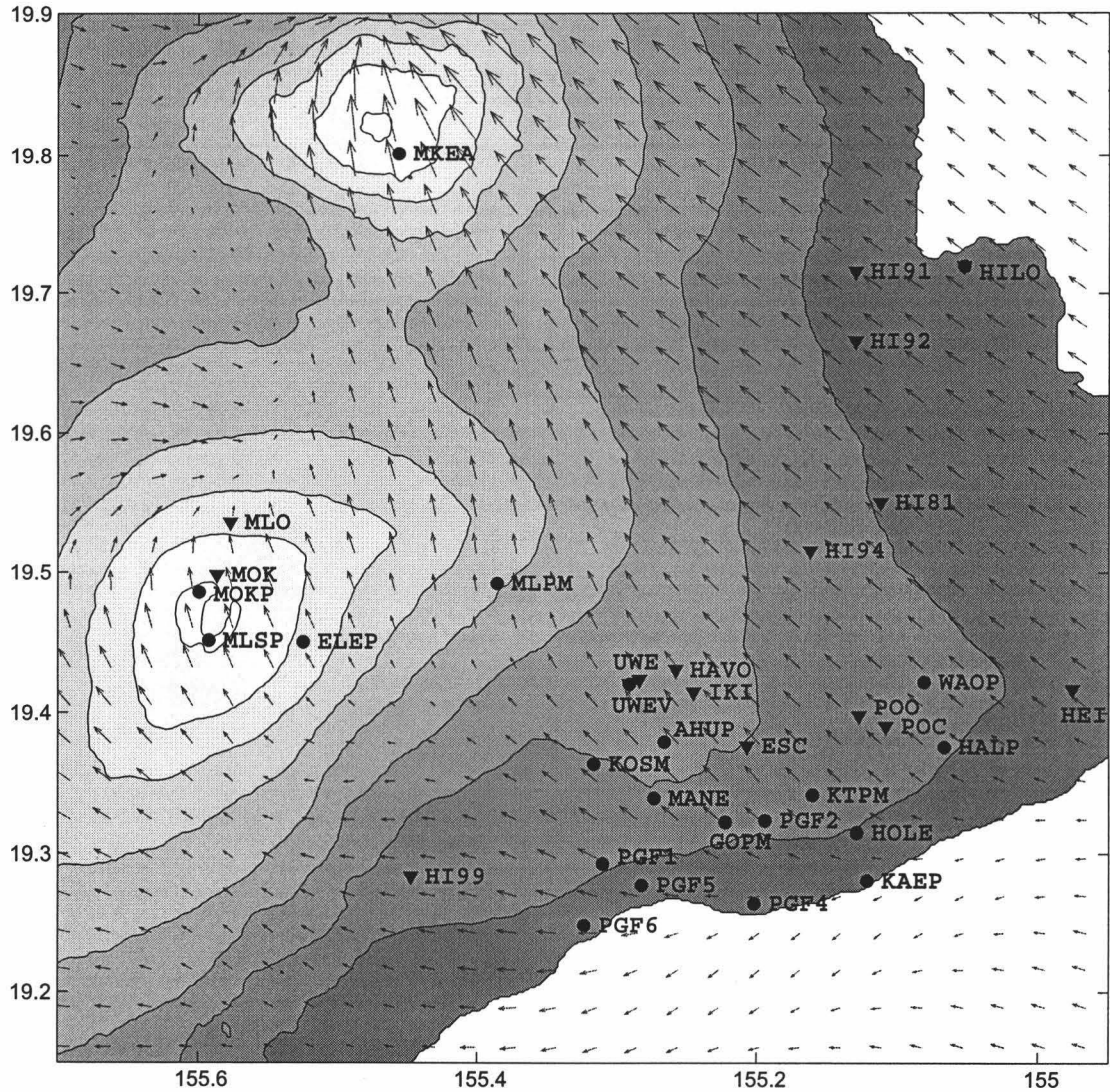


Figure 4.1. Location map showing the GPS sites and rain gauges used in this study. Rain gauges are marked by triangles, GPS sites by circles. The MSM-modeled surface wind field for 0000Z 3rd November (day 308) is overlain in dark gray arrows to illustrate the regional wind field for the storm event.

Introduction

The Ka`ū (pronounced Ka-oo) Storm was an extreme rain event that impacted the south and east sides of the Big Island of Hawai`i during the 1st and 2nd of November, 2000. Maximum hourly rain-rates were over 100 mm/hr (~4 in/hr) and the total rainfall from the storm reached nearly 1000 mm at one location, with a 24-hour accumulation that fell just short of setting a state record. Stream gauge records show that this was the most intense, widespread rain event in 20 years, and at several sites the maximum stream-flow from this storm established records. The extensive flash floods that resulted are estimated to have caused \$70M property damage and the impacts on roads and other infrastructure persisted for weeks afterwards. Intriguingly, several days after this huge water-load was deposited on the island GPS sites recorded the first documented instance of an aseismic slip event on Kīlauea Volcano [Cervelli et al., 2002]. This suggests that a shallow fault may have been activated by the increased pore-pressure due to this excess of water, and raises the question of whether landslides might also be a delayed but significant hazard from extreme rainfall events in this area.

The storm was fueled by the remnants of Tropical Storm Paul, which developed in the inter-tropical convergence zone off the west coast of Mexico on 22nd October. Paul is estimated to have become a tropical storm on the 26th and to have largely dissipated by the 29th, having traveled about halfway to Hawaii. The remnants continued westward and, as they approached the Big Island on 1st Nov., they were amplified by an upper level trough located to the west of the islands.

The maximum rainfall was recorded by the rain gauge at Kapāpala Ranch on the south slope of Mauna Loa (Figure 4.1). This gauge recorded 989 mm (>39 inches) of rain over 36 hours and heavy rainfall was recorded over most of the southern and eastern

portions of the Island. Previous studies have investigated this pattern of heavy rain event on the south-facing slopes of Hawai'i [Kodama and Barnes, 1997; Schroeder, 1978] and have interpreted the large temporal scales of the heavy precipitation and the quasi-stationary nature as the effect of orographic lifting which anchors the storm to the mountainous terrain when the winds are blowing onshore.

The formation of the deep convection required for heavy rain is controlled by the depth of the moist layer depth and the interaction of the surface winds with the islands' complex topography. The NCEP Global Spectral Model, which, with about 1-degree grid spacing, does not include topography for the Hawaiian Islands, failed to predict any of the subsequent rainfall. The more detailed Regional Spectral Model (10-km grid) run operationally by NWS/U.H. Dept. Meteorology [Wang et al., 1998] which incorporates coarse topography was able to predict some rainfall, but it was both grossly underestimated, and mislocated. Only with the inclusion of detailed topography in a 3-km grid Mesoscale Spectral Model [Zhang et al., 2000; <http://www.soest.hawaii.edu/~rsm>], run after the event, was a more realistic model of the actual rainfall generated although even then the predicted rainfall was only 50-60% of the actual measured values. This highlights the potential contribution that an all-weather GPS system could make in providing rapid and accurate precipitable water (PW) estimates, particularly in concert with satellite data, for which GPS could provide point PW calibrations [Motell et al., 2000].

A network of GPS receivers (Figure 4.1) covers much of Kīlauea and the summit of Mauna Loa, allowing us to calculate frequent, accurate estimates for the precipitable water over much of the area most affected by the storm. With sites at elevations from sea level to over 4000 m at the summit, and with an average spacing of less than 10 km this network provides us with a unique opportunity to examine the details of the precipitable water distribution as the storm passed over the southeastern section of the island.

This paper has two main objectives. First the details of the precipitable water field are examined to better understand the evolution and structure of these extreme events. The possibility of using the GPS PW estimates as a proxy for rainfall is then explored, and the GPS-predicted rain-rates are compared with those modeled by the MSM and observed at the rain gauges. This case study is intended to help in assessing and extending the capability of GPS to provide raw data and information that can be interpreted without the necessity of incorporating it into a full meteorological model. With the rapid proliferation of GPS-Met capable systems globally and their relative affordability it is of value to investigate what information can be gathered and interpreted from the GPS as a stand-alone meteorological instrument, especially information that is of importance to hazard monitoring and mitigation.

Network and Data Methodology

Bevis et al. [1992] first pointed out that the increasingly sophisticated models of the tropospheric refraction required by GPS geodesists in order to obtain millimeter accuracy for positioning could be used to derive an estimate of the total column water vapor content of the atmosphere, or precipitable water (PW). By using a model of the elevation dependence of the delay in the troposphere [e.g. Neill, 1996] a time-varying estimate of the total equivalent zenith delay (ZND) can be calculated during the GPS processing. There are two main components to this delay: hydrostatic (or “dry”) and “wet” (water vapor). The hydrostatic delay (ZHD) is proportional to the mass of the atmosphere above the site and so can be predicted accurately by surface pressure measurements [Saastamoinen, 1972]. The much more variable wet component (ZWD) can then be determined by subtracting the ZHD from the estimated ZND. In order to convert the ZWD estimate into a measure of PW the mean-weighted temperature of the atmosphere is needed. Studies by Bevis et al., [1994] Duan et al. [1996], and Ross and Rosenfeld [1997; 1999] show that this can be predicted to sufficient

accuracy from surface temperature measurements, and a mapping parameter “ π ” can be calculated that maps the ZWD into PW. Various subsequent studies have confirmed that the final GPS derived estimate of integrated PW is of comparable accuracy to traditional meteorological instruments such as water vapor radiometers and radiosondes [e.g. Tregoning et al., 1998; Gutman et al., 2001]. As GPS is a relatively cheap, all-weather system, it has become increasingly attractive option for augmenting meteorological networks, and several countries are starting to fully incorporate GPS data into their weather-models [e.g. Gutman et al., 2001; Dick et al. 2001].

The Pacific GPS Facility (PGF) installed a network of 6 GPS receivers on the South Flank of Kīlauea Volcano during the summer of 1996 and later added an additional site at the National Weather Service Office in Hilo. A sister network of 15 receivers was installed by the USGS Hawaii Volcano Observatory and Stanford University on Kīlauea and Mauna Loa for volcano-deformation monitoring. An additional receiver on Mauna Kea is run by JPL. The combined networks give dense coverage of the Kīlauea area from sea level to over 4000 m at the summit of Mauna Loa. With the passing of the Ka`ū Storm over these networks we have the opportunity to image the precipitable water distribution within this extreme weather system in unprecedented detail.

Although the spatial coverage of the GPS receivers is very good, only the PGF (PGF1, PGF2, PGF4, PGF5, PGF6 and HILO) and JPL (MKEA) receivers (see Figure 4.1) have collocated meteorological instruments to provide the surface pressure and temperature measurements needed to directly estimate the PW. Hawaii is famous for its microclimates [Juvik, 1978] due to the orographic effects of the huge volcanoes. Rainfall in particular varies dramatically over very short horizontal distances [Giambelluca, 1986] but all surface meteorological parameters are affected and have complex local variations. The extreme relief

across the GPS network compounds this problem, making it very difficult to accurately extrapolate pressure and temperature fields any distance from the measurement points.

The solution that we adopted was to include data from the NCEP Reanalysis. Pressure, temperature and dew point were interpolated from the reanalysis to each GPS site. The coarse (1 degree) grid for the reanalysis is naturally unable to reproduce the details of the island's meteorological patterns, however the mean values for each site predicted from this grid were typically very close to the mean measured values; not surprising, as to a first approximation we are simply located in the middle of the ocean. A correction field for the NCEP-predicted data was calculated by modeling the misfits between the observed data and the NCEP-predicted data using linear spatial gradients and offsets. As the magnitudes of the misfits from the measured data are small, the exponential form of the pressure can be ignored and all the fields treated as behaving linearly, simplifying the procedure. These final predicted data, interpolated to the GPS atmospheric knot epochs match the measured data to \sim . 25 mbar and \sim 1.5 deg-C rms while preventing the extrapolated fields from tending to unrealistic values away from observation points. The accuracies typically required for pressure and temperature data for use in GPS meteorology are 0.3 mbar [Saastamoinen, 1971] and 3 deg-C [Emardson and Derks, 2000] indicating that the extrapolated fields are sufficiently accurate for this study.

GPS data from the all of the Big Island sites running during the storm were processed using a sliding window technique [Fang et al. 1999]. In this technique a moving time window is used to select data for processing. Although this technique can be used with no sequential window overlap in order to minimize the processing time, allowing a significant overlap for each window has the advantage of producing several estimates for each time epoch. These multiple estimates allow for an internal check on the accuracy of the solution, and allow us to find a robust average for each epoch. This also avoids a problem that plagues the more

traditional batch processing where the switch from one 24-hour orbit solution to the next causes a “boundary effect” at the poorly constrained window edges where sequential solutions appear to be offset from each other at their common epoch. The processing package GAMIT [King and Bock 2000] was used along with precise orbits solutions from the Scripps Orbit and Permanent Array Center (SOPAC) to generate solutions for the 10 days covering the storm. The processing window was 8 hours wide and stepped forward in hourly increments, with atmospheric estimates made every 15 minutes using a piecewise constant function.

Internal consistency checks of the GPS atmospheric solutions suggest that the final ZND estimates are accurate to better than 10 mm. External checks are more problematic: the NWS radiosonde launches in Hilo failed during the storm (incidentally illustrating one of the advantages GPS has over many of the traditional meteorological instruments) and although there is a second Hawaiian NWS radiosonde launch site in Līhu`e, Kaua`i, the GPS receiver at the site was, unfortunately, not operational during this period. As no local independent verification of the GPS estimates was possible for the storm event we have to rely for our error estimates and on previous experience. Motell et al. [2001] found that the rms difference between PW from the Līhu`e radiosonde and the GPS site was ~1.7 mm. As a significant component of that difference must be due to errors in the radiosonde PW retrieval, and studies of GPS PW accuracy elsewhere indicate similar or better accuracy [for example, Tregoning et al., 1998; Fang et al., 1998] we conclude that the absolute accuracy for those sites with surface meteorological data is ~1.5 mm of PW while for the other sites the combined errors in the GPS solutions and surface meteorological field extrapolations translate to an accuracy of ~2 mm of PW.

The National Weather Service installed an automatic rain-gauge network across Hawaii in 1995. These Hydronet sites report accumulated rainfall hourly. The HVO also has

rain gauges attached to its network of volcano monitoring tilt meters (rainfall strongly affects measured tilt). In addition the National Park Service AIRS program maintains rain gauges within the National Park, and the NOAA Mauna Loa Observatory site measures rainfall just below the summit of Mauna Loa. These sources provided a network of 16 gauges with hourly rainfall data in and around the GPS network active during the storm.

Results

Temporal Structure of the Precipitable Water

Figure 4.2 shows a montage of precipitable water time-series from 5 GPS sites. From PGF6, located near sea level on the south shore of Kīlauea the sites step upslope, roughly northwards to MLSP on the summit of Mauna Loa. The bottom panel shows the rain gauge record for Kapāpala ranch, the location of the highest recorded rainfall for the storm, and located slightly to the west of this profile.

The five traces show the same general pattern for the storm, imaging a strong initial drying event followed by a rapid rise in PW with the high maintained through the night of 1st to the 2nd of November. In detail, however, there are several interesting differences. The preliminary drying event, and the subsequent rapid rise in PW during morning of the 1st occurs later at the higher elevations: the trough at MLPM reaches a minimum a little after the lower three sites and persists longer. At MLSP, well above the inversion layer, on the summit of Mauna Loa, the PW is actually still rising slightly when the lower sites reach their minimums (time “a”), before showing a brief, small trough while the others have already begun to climb strongly. The drying event is probably related to subsidence in front of the approaching storm, perhaps enhanced by the diurnal katabatic flow as the island cools during the night [Feng and Chen, 2001].

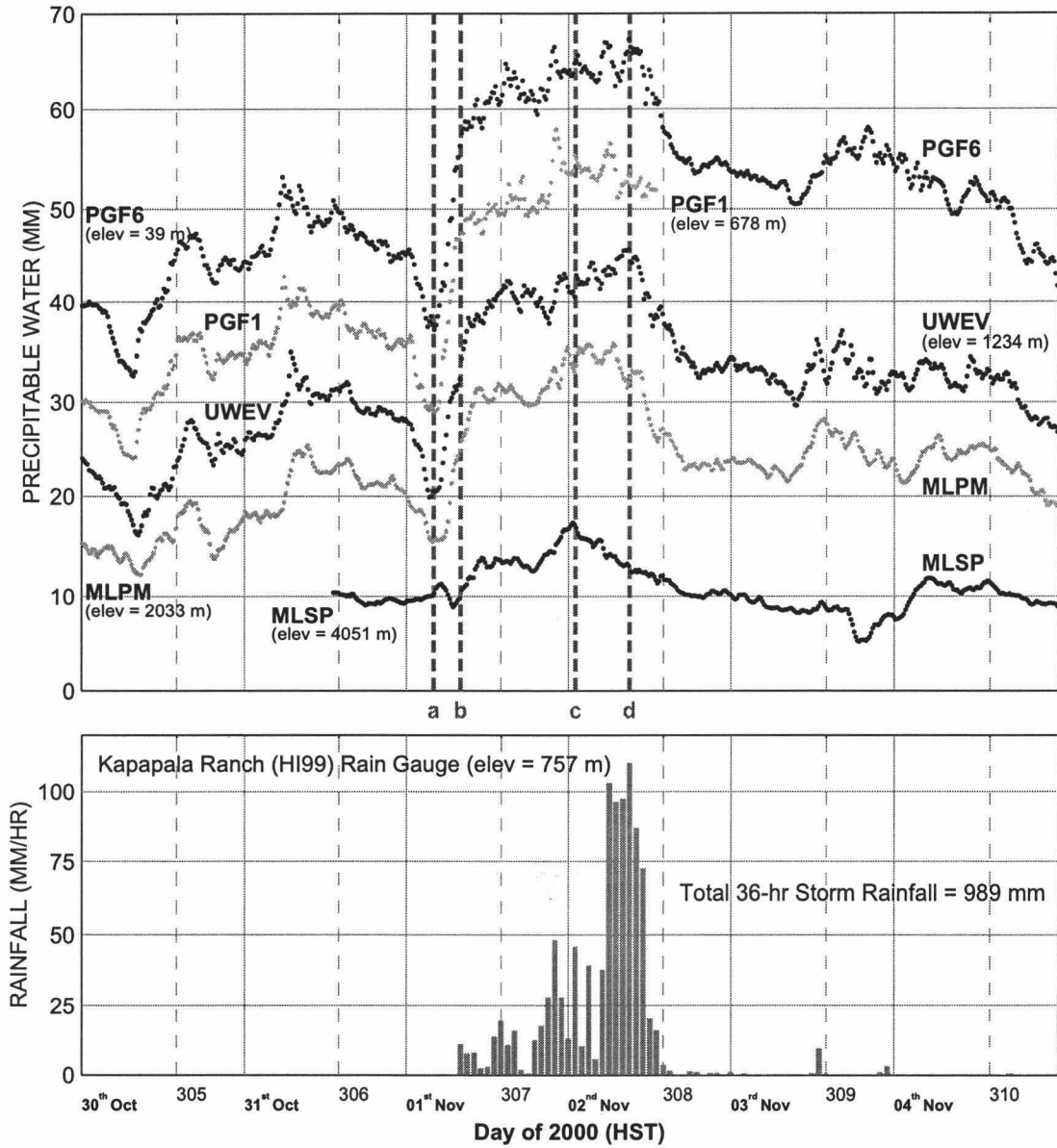


Figure 4.2. a). Five GPS-derived precipitable water time series representing a vertical profile from sea-level at PGF6 to MLSP at 4050 m on the summit of Mauna Loa. Also shown as the lines marked a-d are the four times for which map-views are presented in Figure 3. b) Rainfall from Kapāpala Ranch, to the west of the GPS transect and site of the highest measured rainfall for this event.

Notably, while the lower sites continue to see an increase in PW until mid-morning of the 2nd of November, MLPM starts to decrease earlier, and MLSP (and HILO; see Figure 4.6) reached its peak values at about midnight and declines throughout the day. The rain data reflect the same pattern with rainfall at Kapāpala Ranch peaking mid-morning, and rainfall at Hilo and Moku`āweoweo peaking at midnight. This suggests that there were two main rainfall episodes, the first primarily affecting Hilo and the north-eastern slopes of Mauna Loa and the second more locally focused on the south-eastern slopes at the western edge of the GPS network (the Ka`ū district).

The details of the sub-peaks that are superimposed on the broad PW high are subtly different between all the sites, probably reflecting the small-scale variability inherent in the atmosphere. Although some of the peaks are clearly correlated between sites, for others correlations are less obvious, illustrating the small-scale structure of PW field.

The PGF1 time-series is a dramatic testament to the flash floods that accompanied the peak rainfall of this event. PGF1 is located several meters above a storm stream channel. The abrupt end of its time-series, shortly after the peak rainfall recorded at Kapāpala Ranch, records when the floods become so intense that they inundated the surrounding area and washed the GPS receiver box down the hill, ripping out the antenna cable and short-circuiting the electronics. The receiver was recovered near the lip of a ~1000 ft cliff, was repaired and the data were recovered. PGF6 located on the coastal plain below PGF1 and near the edge of the alluvial fan deposited by such flood-events narrowly avoided a similar fate.

Spatial Structure of the Precipitable Water

To examine the spatial structure of the PW field, the PW estimates need to be gridded. In order to perform a robust 2-dimensional gridding we first need to remove any

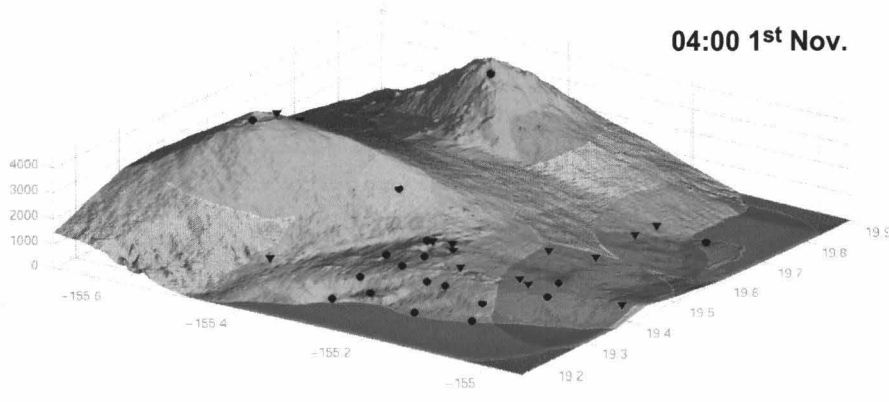
explicit elevation dependence of the data. We achieve this by first removing an exponential fit to the long-term elevation dependence of the median PW values for each site. This long-term trend is calculated from all the available data from 1997 through the end of 2000. The residuals from the long-term median fit have a linear elevation dependence, so our final step in the data preparation is to calculate and remove another, this time linear, elevation fit. Horizontal trends are also calculated and removed, leaving us with a trend-free set of residuals with zero mean.

The residuals are then fitted using double Legendre polynomial series with the orders of the series expansions chosen subjectively using singular value analysis [Lawson and Hanson, 1974]. This allows us to examine directly the trade-off between fitting the data values as closely as possible and the tendency of the fitting functions to become poorly constrained oscillate wildly in the data gaps. In order to help stabilize this procedure extra pseudo-data were added in a coarse grid. As the mean, or expected value of the PW residuals being gridded was zero, a coarse grid of zeros was added, down-weighted, allowing the real data to control the solution but helping to constrain it to zero away from the data points. This procedure helped to minimize edge instabilities while allowing a sufficiently high number of degrees of freedom to provide a close fit to the data. In general the RMS misfit of the polynomial models to the data is less than 1 mm PW. Once the polynomial fit has been selected, the polynomials are re-evaluated over the entire grid and the previously calculated PW trends reintroduced via a digital elevation model for the area.

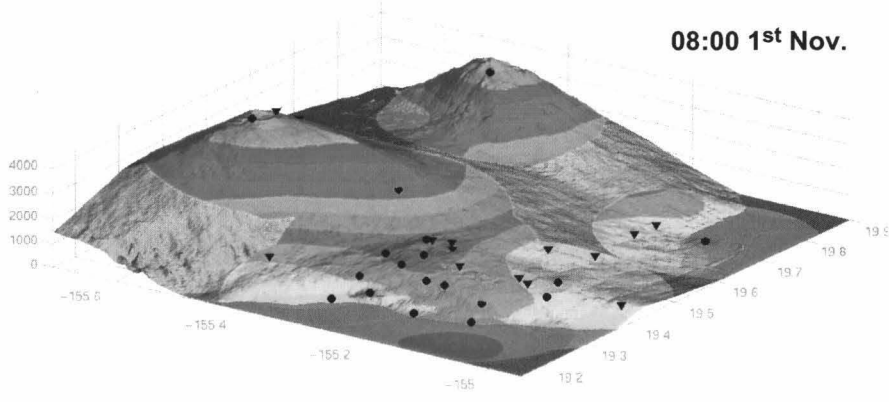
Using the absolute value of the PW results in maps that strongly reflect the topography, making it difficult to discern any relative differences in the spatial distribution. To show more clearly the relative PW abundance, the difference in PW from the long-term median trend is plotted (Figure 4.3). Here there is still elevation dependence, but it is possible now to see some of the detail in the relative abundances. The influx of low-level moisture can

Figure 4.3. Map views of precipitable water estimates for the epochs (a-d) marked in Figure 2. a) 04:00 (HST) 1st Nov, during the precursory drying event. b) 08:00 (HST) 1st Nov, all sites show a rapid rise in PW. c) 01:00 (HST) 2nd Nov, as the Hilo and high-level PW peaks, and d) 09:00 (HST) 2nd Nov, as the low level PW on the south slopes of Kīlauea peaks and Kapāpala Ranch records its maximum rain rates. (Note that the Mauna Kea station went offline sometime after the peak of the storm.)

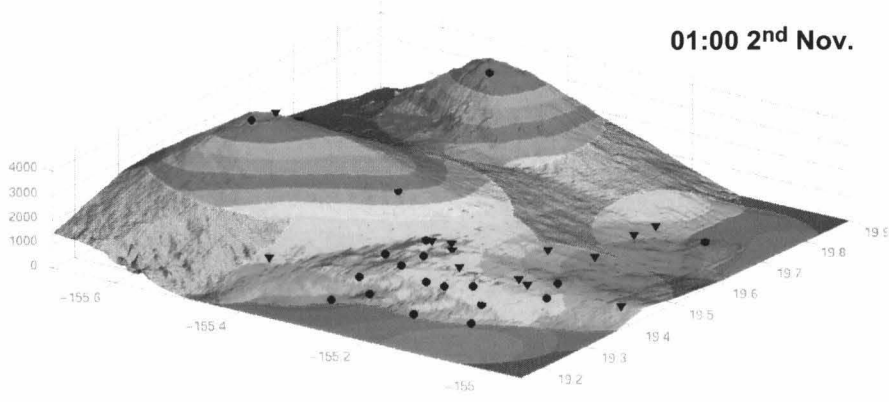
04:00 1st Nov.



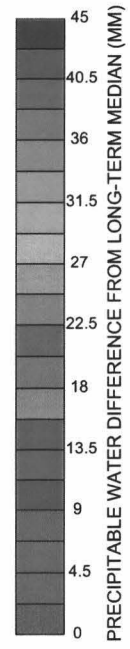
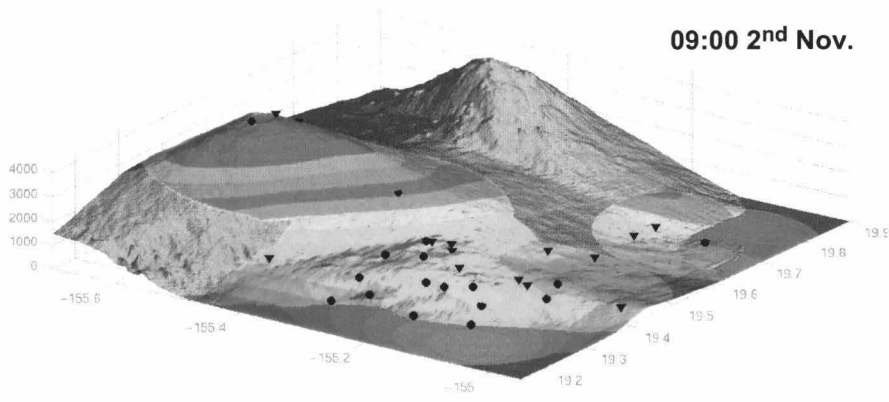
08:00 1st Nov.



01:00 2nd Nov.



09:00 2nd Nov.



be clearly seen as the PW at lower elevations rises from near its long-term median values while the peaks of Mauna Loa and Mauna Kea remain relatively unchanged (Figure 4.3a & b). As the moist layer thickens and the convective systems become established, the volcano peaks finally also register PW values well above average (Figure 4.3c & d).

Simply removing the median value is not enough to remove all the elevation dependence and the correlation of the PW residual with topography is still clear in Figure 4.3 since the variation from the median is also a function of height. Foster et al. [2002] show that the long-term variability of PW in Hawaii closely approximates a lognormal distribution. A lognormal distribution is characterized in terms of its median (M) and its geometric standard deviation (GSD) [Aitchison and Brown, 1957]. We define the normalized variability of PW (NPW) at a site in terms of the number of (geometric) standard deviations from its long-term median value:

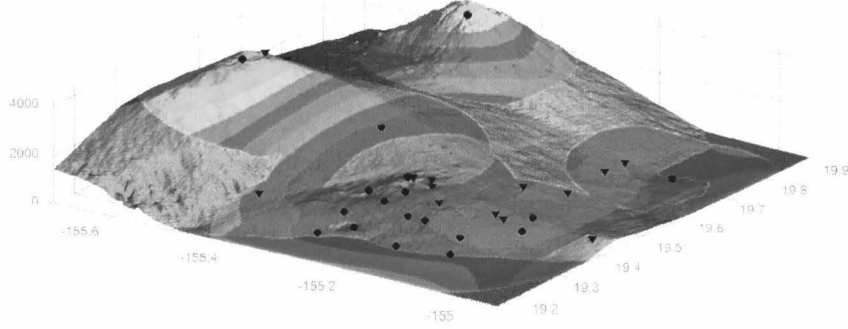
$$NPW = (PW - M_{PW})/GSD_{PW}$$

where M_{PW} and GSD_{PW} are the median and the GSD of PW at the site. This number is intrinsically height-independent and so provides a flexible basis for the representation and gridding of precipitable water. Note that although these standard deviations are derived from the absolute PW, they themselves do not directly represent a physically meaningful measure of the atmosphere, however we believe they do provide a useful way of visualizing the relative PW abundance in areas with large topographic relief.

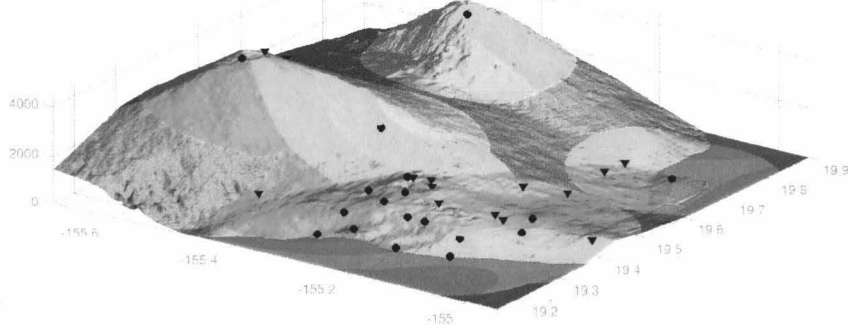
Imaging the same epochs using this approach (Figure 4.4) highlights the excess NPW at the higher elevation on the summits of Mauna Loa and Kīlauea (Figure 4.4a), with a relative low over the western part of Kīlauea and the lower south flanks of Mauna Loa. A single patch of slightly higher NPW is located mid-way down the East-Rift Zone of Kīlauea. During the phase of rapid PW increase (Figure 4.4b) we see a broad regional rise with little

Figure 4.4. Maps showing the normalized variability of PW (NPW) for the same epochs as Figure 4.3. $NPW = (PW - M_{PW})/GSD_{PW}$. M_{PW} is the long-term median PW value at a site and GSD_{PW} is the long-term geometric standard deviation.

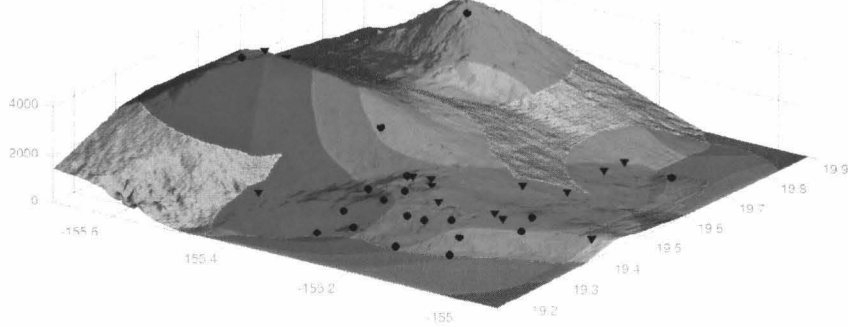
04:00 1st Nov.



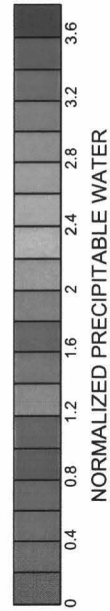
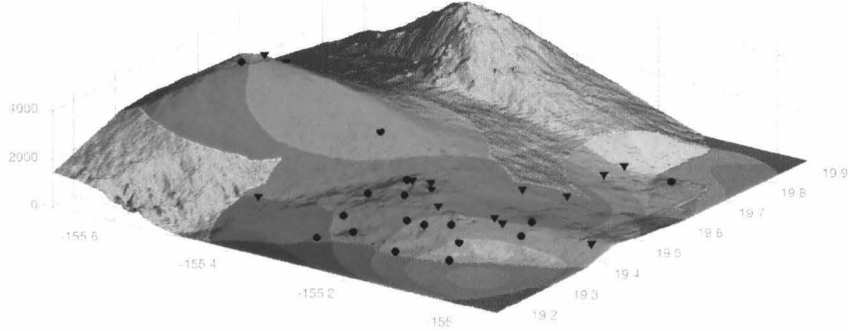
08:00 1st Nov.



01:00 2nd Nov.



09:00 2nd Nov.



variation across the network except for the same relative high on the East Rift Zone, now a little further north towards Hilo. The summits now have a NPW levels similar to the lower areas.

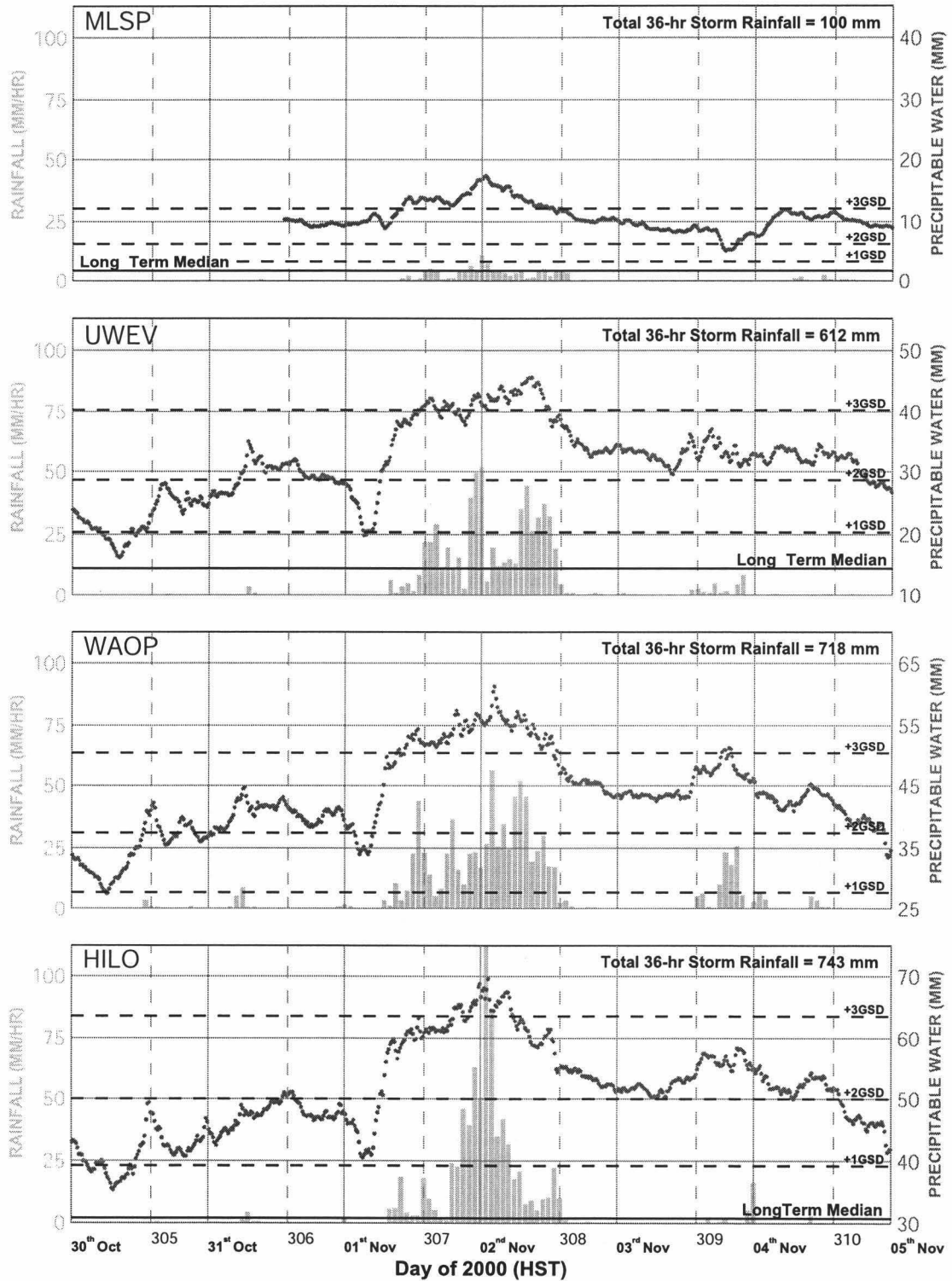
During the peak of the first main rainfall episode (Figure 4.4c) the NPW pattern shows excess PW concentrated over the summit and south slopes of Mauna Loa and extending over the saddle with Kīlauea towards Hilo. This is the zone of highest precipitation and the area where onshore winds blowing directly upslope (Figure 4.1) promote uplift, and anchor the system to the side of the volcano. The incoming flow may also decelerate as it encounters the island obstacle, leading to convergent airflow offshore.

In the final panel (Figure 4.4d) we see that the NPW is declining at most locations, especially the summits. Despite this general decline, this was the period of most intense rainfall measured at Kapāpala Ranch indicating that although less moist air is being uplifted above the summit area of Mauna Loa, there is still intense localized convergence on the lower slopes. A NPW high can be seen below the Kapāpala Ranch gauge: it seems likely that this NPW high actually extended further inland but, as there is no GPS site close by, the PW for this area is not well described by extrapolation from the Kīlauea sites for this period.

Precipitable Water and Rainfall

There are 4 GPS sites in the network that have rain gauges located within a few kilometers. As the GPS antennas and rain gauges are close to each other we can reasonably assume that they recorded the same events at the same time, giving us the opportunity to examine in detail the relationship between the PW and rainfall (Figure 4.5). These 4 pairs constitute an east-west profile from near sea level at Hilo to ~4050 m at the top of Mauna Loa. The total rainfall for these gauges for the 36 hours of the event ranges from 100 mm (~4

Figure 4.5. Four GPS and rain-gauge site-pairs showing the relationship between the precipitable water and rainfall time-series. (MLSP was used instead of MOKP, which is closer to the rain gauge, because MOKP was not active until after the main storm event had passed.) In addition to the absolute PW, the long-term median PW values and the +1, +2 and +3 standard deviation values are shown. The vertical range for the 4 panels has been chosen to provide the same vertical scaling for the PW.



inches) on the summit of Mauna Loa to 785 mm (~30 inches) in Hilo, with the peak rainfall occurring during the night of Nov 1st and early morning of Nov 2nd local time (HST=UTC-10). The first significant rainfall occurs during the rapid PW rise during the early morning of 1st Nov. as the moist air first reaches the island. The rain typically begins as the PW reaches between 2 and 3 GSD above the median and increases in intensity with increasing PW. The PW climbs to a high plateau, with levels typically more than 3 standard deviations from their long-term-median values, and over the next 24 hours the PW shows small, short-period peaks superimposed over this plateau. In many cases these spikes appear to be correlated with increases in the rainfall at the nearby rain gauge, although the size and duration of these rain-spikes is less clearly related to the size of the PW spikes. Finally the PW starts to fall, with rain largely ceasing by 14:00 on the 2nd as the PW drops below 3 GSD. The slow PW decline back towards median values is interrupted on Nov 3rd by a brief peak at the three lower sites that is uncorrelated with significant rain at any of these except WAOP.

Comparing the rainfall records of the four sites, it can be seen that although the drying and subsequent rapid increase in PW is roughly contemporaneous at the three low elevation sites, as is the onset of the rain at all sites, the timing for the peak rates of rainfall differs across the network. HILO shows a small initial rain event, followed at sundown (~18:00) by sustained high intensity rainfall through the night, dropping off at sunrise (~06:30) with one last burst mid-morning. In contrast the two mid-level sites have higher rates during the initial onset, and their most sustained intense rainfall occurs later, around dawn. The highest site, MLSP, has its peak rainfall at midnight, closely tracking the PW, but is then relatively constant until it finally stops mid-afternoon on the 2nd.

The apparent correlation of many of the rainfall peaks with precipitable water spikes suggests that it may be possible to convert the PW into an estimate of rainfall. We have already normalized the elevation dependency of the PW by expressing it as the number of

GSDs from a long-term median. As the rainfall is also elevation dependent it too needs normalizing in order to examine its relationship to the PW. Figure 4.6 shows the total accumulated rainfall for the storm plotted against the elevation of the gauge. The four gauges shown in Figure 4.6 fall coincidentally on a well defined line and so a linear, least squares fit to this groups of sites was chosen as a representative function for normalizing rainfall by elevation. This form of elevation dependence would only be expected during active convection where there is no inversion layer, but as this is precisely the type of event that produces heavy rainfall this is not an impediment.

Examining the relationship between PW and rainfall (Figure 4.7) shows that although there is broad scatter for low-rainfall events, for each site significant rainfall starts at NPW levels above 1.75 GSD above normal, with rates non-linearly dependent on NPW above this point. Once the NPW reaches 3 all sites show rainfall. Note that Hilo records heavy rainfall at NPW levels than the other sites. This may be partly due to sensitivity to the exact value of the geometric standard deviation when mapping from measured PW to the NPW, or may simply reflect the inadequacy of this method to fully represent the physical processes. The consequence of the onset of heavy rain at Hilo for lower standard deviation levels is that it will be under-modeled when NPW is mapped to rainfall.

The lack of correlation at lower rain rates is not surprising and is probably due to a combination of factors. Previous work [e.g. Chen and Nash, 1994] has shown that normal showers on the Big Island are formed by the combination of early morning (late evening) upslope (downslope) winds and the regional winds. Showers formed this way are not closely related to the absolute PW in the atmosphere but are controlled by local topography and wind convergence. For these showers we would not expect PW to be more than very weakly correlated. In addition to this, it is important to remember that GPS PW estimates represent a mean equivalent zenith value for all the ray-paths measured over the time window of each

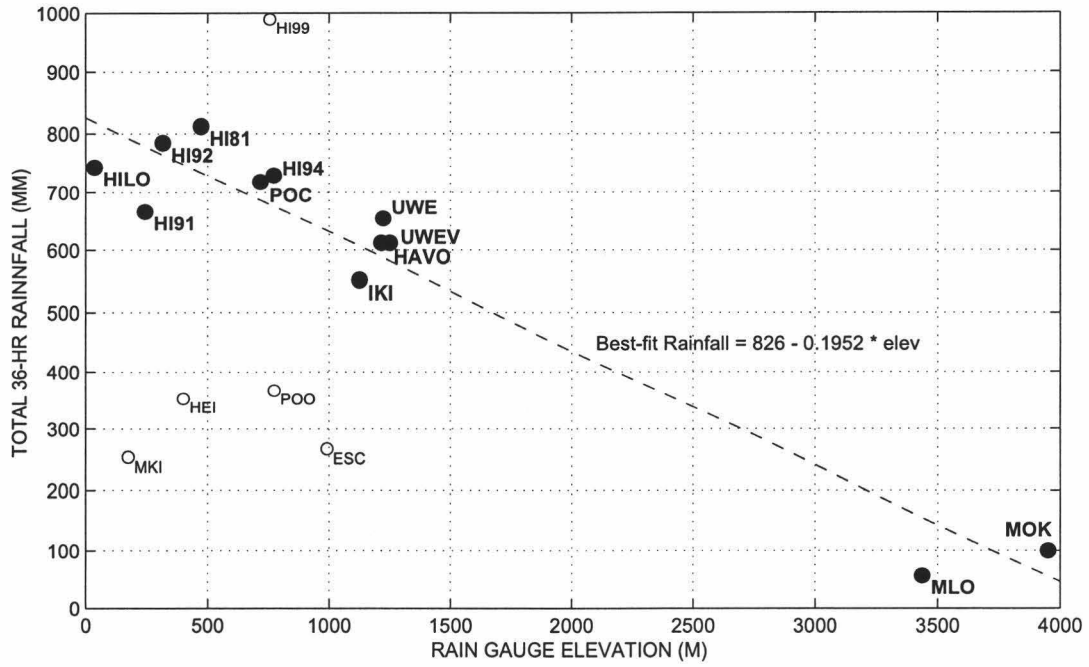


Figure 4.6. Plot of total rainfall for this event against elevation of the gauges. The four gauges chosen in Figure 4.5 for their proximity to GPS sites fall within well-defined group shown with the larger filled circles. This group is chosen to represent the regional relationship with the function: $RAIN = 826 - 0.1952 \times ELEV$.

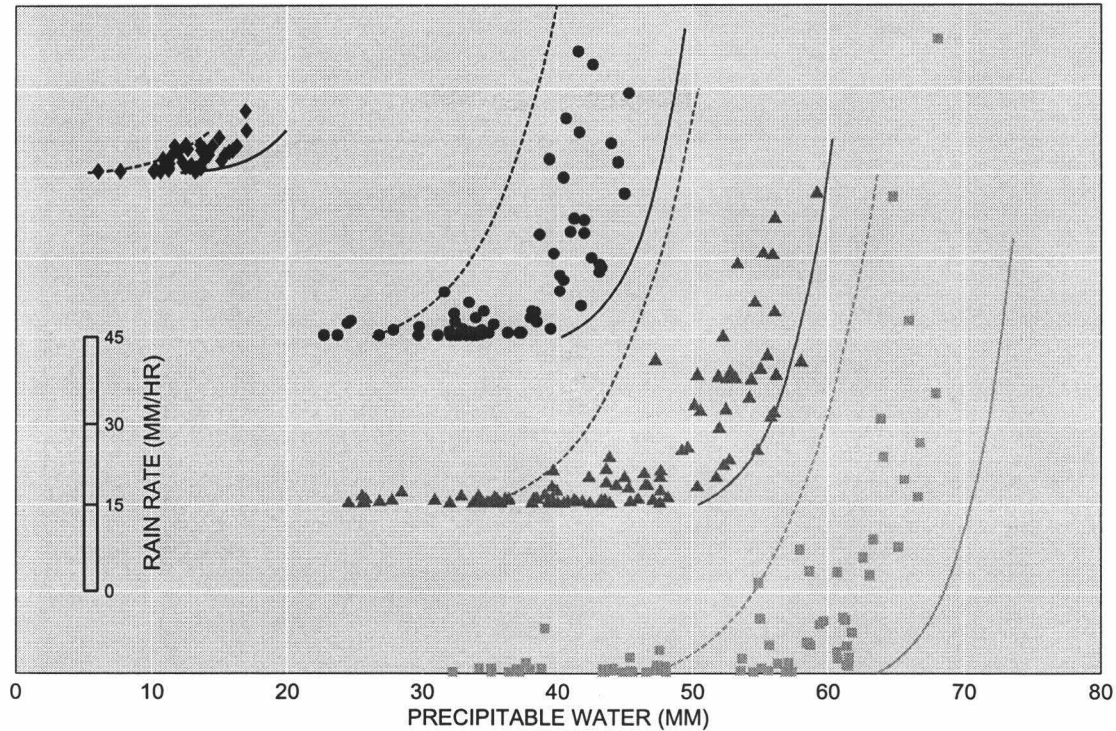


Figure 4.7. Scatter plot showing rain rates vs. precipitable water for the four site-pairs in Figure 4.5: MLSP/MOK (diamonds), UWEV/UWEV (circles) WAOP/POC (triangles) and HILO/HILO (squares). The 4 data sets have been displaced vertically for clarity and the vertical (rain rate) scale is shown. The empirically determined bounds to the data are shown as dotted and solid lines. The lower bound (dotted line) is described by the equation

$$\text{RAIN} = (826 - 0.1952 \times \text{ELEV}) \times (-0.005 + 0.005 \times \exp(2.5 \times (\text{NPW} - 1.75)))$$

and the upper (solid) by:

$$\text{RAIN} = (826 - 0.1952 \times \text{ELEV}) \times (-0.005 + 0.005 \times \exp(5.0 \times (\text{NPW} - 3.0)))$$

Shown as the intermediate dashed line is the chosen representative equation linking rainfall and PW:

$$\text{RAIN} = (826 - 0.1952 \times \text{ELEV}) \times (-0.005 + 0.005 \times \exp(3.75 \times (\text{NPW} - 2.5)))$$

Where NPW is the normalized PW given by the number of geometric standard deviations the PW is above its median value.

solution knot. The GPS PW estimates therefore both spatially and temporally smooth the atmosphere. Small rain events and even most individual convective cells are likely to be somewhat smaller than the area, or “cone of influence,” over which the GPS atmospheric delays are averaged (typically about a 13 km radius), leading to a significant intrinsic underestimate of any smaller-scale PW anomaly over the GPS site. This too would tend to reduce any correlation between GPS PW and low rainfall events.

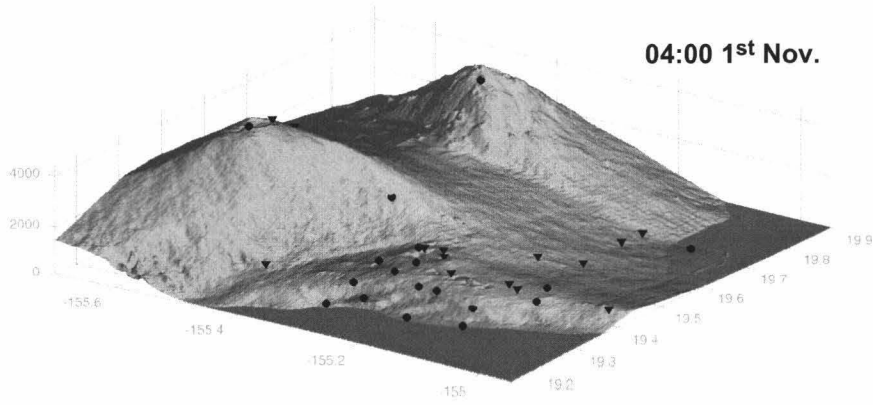
We define an algorithm for estimating rainfall from the PW by ignoring the lower values as argued above, and assuming an exponential form for higher values. The empirically determined formula is given by:

$$\text{RAIN} = (8.26 - 0.1952 \times \text{ELEV}) \times (-0.005 + 0.005 \times \exp(3.75 \times (\text{NPW} - 2.5)))$$

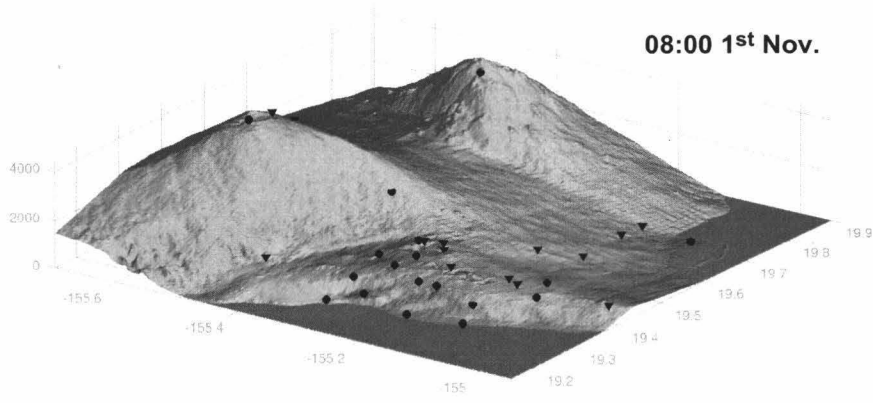
This equation uses 2.5 GSD as its threshold for the onset of rain, and the rate increases exponentially with NPW above this level. In Figure 4.8 we use this algorithm to convert the PW maps shown in Figure 4.4 into equivalent maps of rainfall estimated from the PW. The general patterns of the rainfall naturally follow the patterns for the NPW described in Figure 4.4. Now however the pattern is modulated by elevation, resulting in only small values for the rainfall over the summits and relatively high values at lower elevations. The mapping generates its first rainfall during the rapid PW rise (Figure 4.8b) with low levels upslope of Hilo and on the lower southeast slopes of Mauna Loa. The rain during the PW peak in the early morning hours of the 2nd is concentrated at these same locations, with lower levels over most of the entire area. A gridding artifact is visible on the south rift zone of Mauna Loa where the poorly constrained portion of the mapped field shows very high rainfall. Rainfall drops almost everywhere by the final panel (Figure 4.8d) as the storm passes, except in the area near the Kapāpala rain gauge, which records its highest rainfall at this time. As noted earlier, although the zone of highest mapped rainfall does not quite extend to the gauge location it seems likely that this is due to its distance from the nearest GPS site and that if the

Figure 4.8. Map views of the GPS-derived predictions of rainfall. The equation used to map PW into rainfall is given in Figure 4.7.

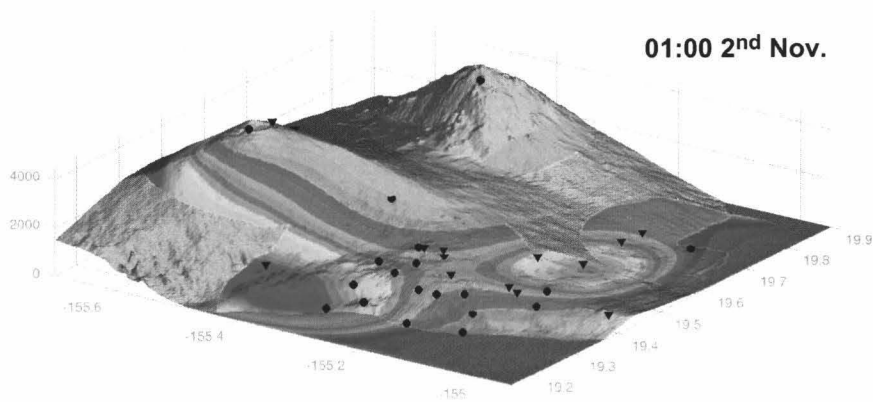
04:00 1st Nov.



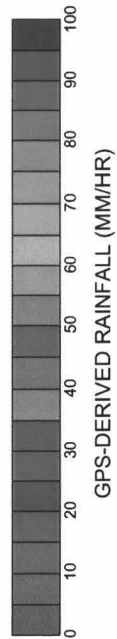
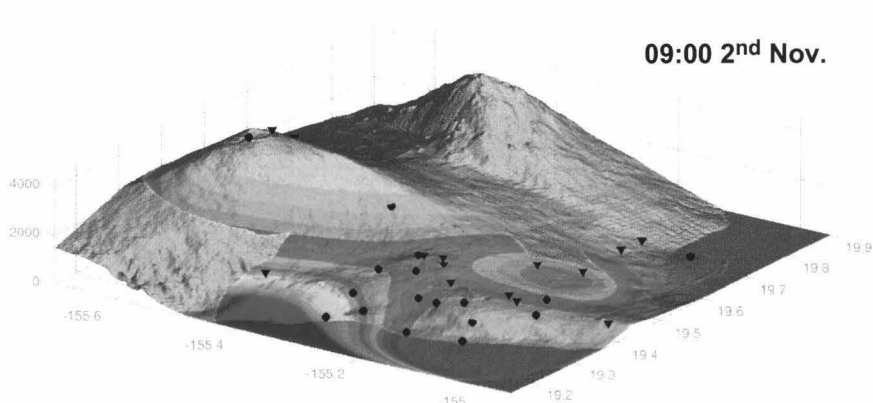
08:00 1st Nov.



01:00 2nd Nov.



09:00 2nd Nov.



PW field was slightly better constrained this extreme rain zone would map a little higher on the slope.

GPS and the Mesoscale Spectral Model

To test the performance of the conversion algorithm, the mapped rainfall was estimated for each rain-gauge location for day 307 for which the MSM was run (Figures 4.9 and 4.10). Accumulated 3-hour rainfall – the time interval for the MSM - is plotted for each of the 3 data sets for all the rain gauges.

The GPS predicted rainfall follows the pattern of PW with most sites showing a general increase until the middle of the day before falling off again. The observed rainfall shows more variation, with several sites experiencing a slight lull in the rain during the middle of the day that the GPS derived field is unable to reproduce. In other cases however the fluctuations in PW that are captured by this conversion do seem to match quite well with the observed rainfall.

Some sites, particularly those on the southeast portion of Kīlauea, are quite poorly matched. The PW maps show a persistent relative low in PW over some of this area (Figure 4.4) however the algorithm still overestimates rainfall for most the day. The Mauna Loa Observatory represents a similar case. Here again the GPS predicts again much more rainfall than is observed. This is probably mainly due to the shadow effect of the summit with the bulk of the precipitation occurring on the upwind (for this event) side on the volcano. At Kapāpala Ranch the late burst of extreme rainfall is not reproduced by the GPS data and it over

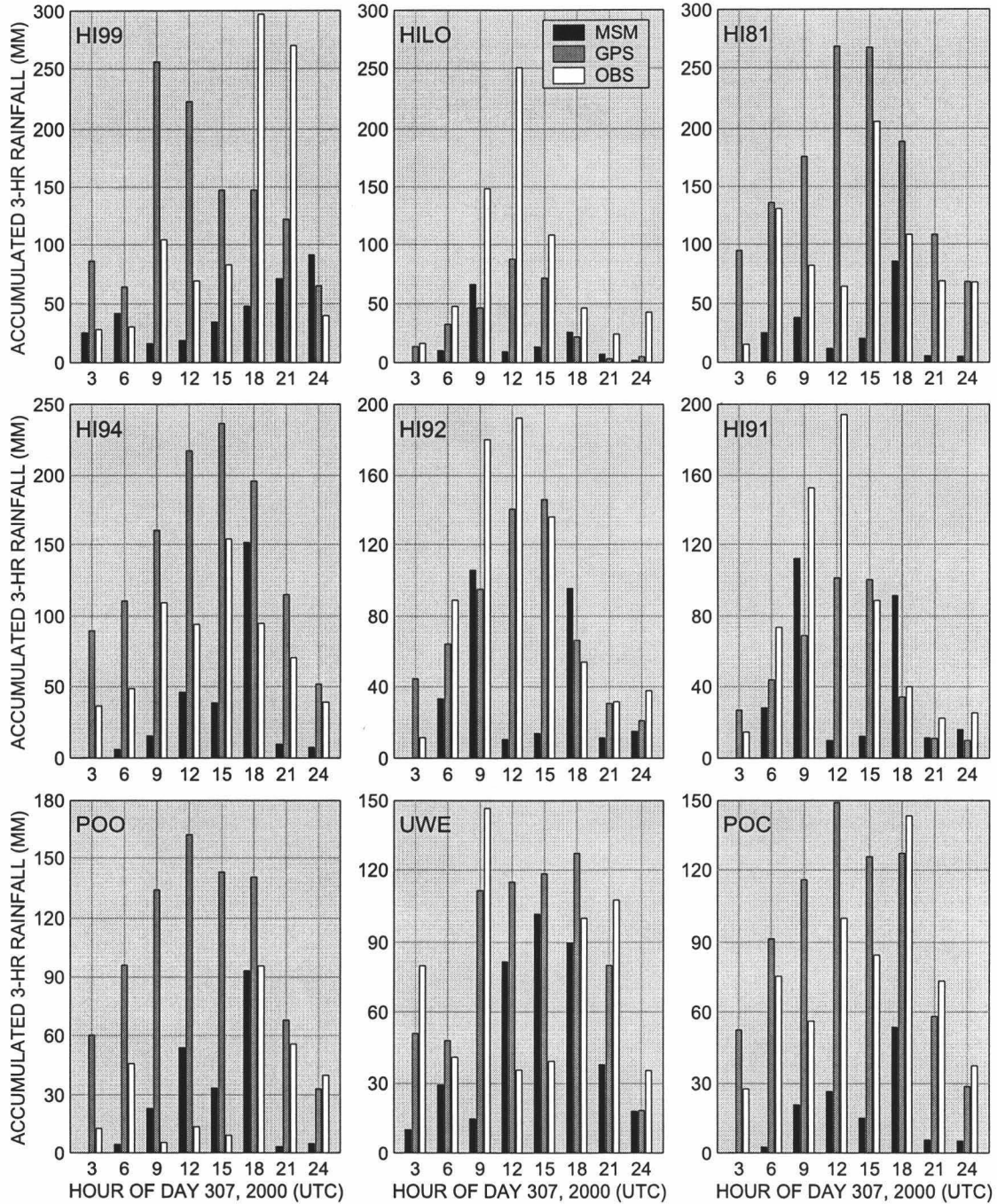


Figure 4.9. Bar graphs of accumulated 3-hr rainfall for UTC day 307 for the MSM and GPS estimated rainfall and the measured rainfall. Gauges 1-9. MSM predicted rainfall shown as black bars, GPS-derived estimates in gray and observed values in white.

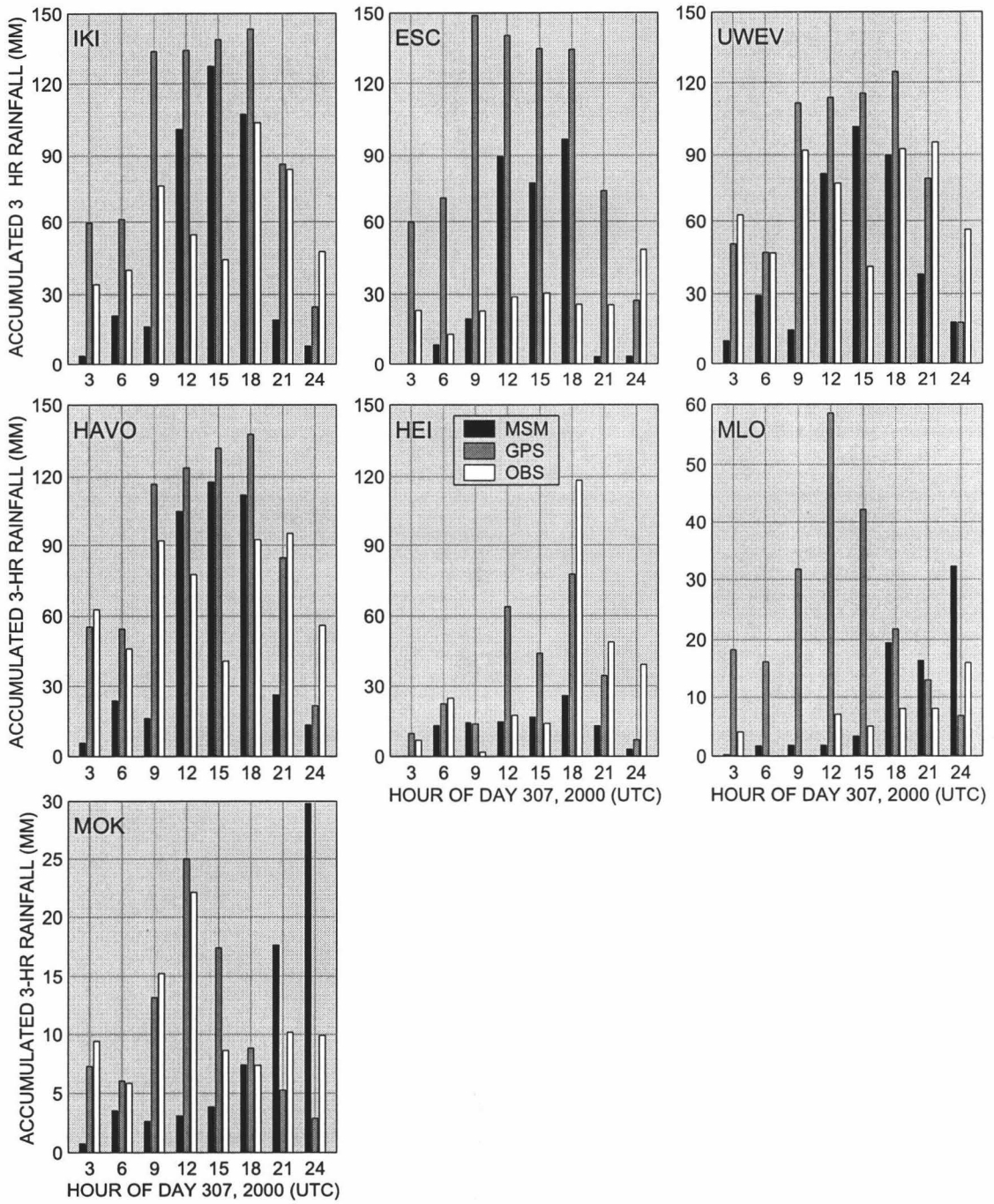


Figure 4.10. See Figure 4.9. Gauges 10-16.

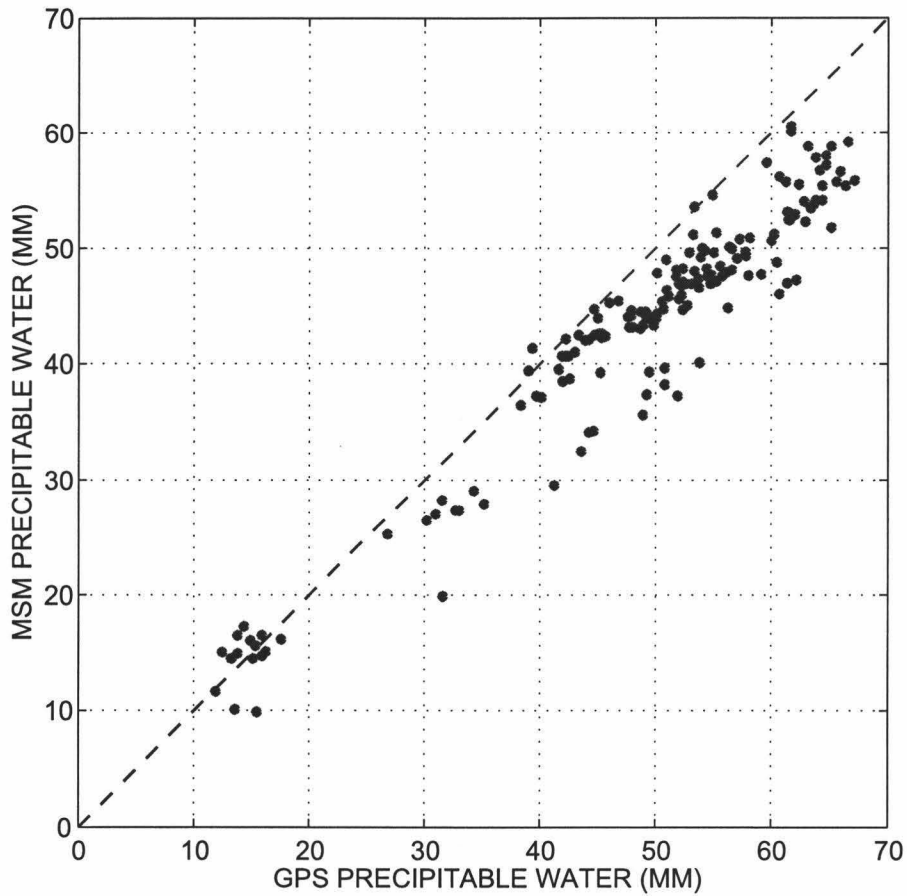


Figure 4.11. MSM predicted precipitable water and GPS observed precipitable water, indicating pervasive MSM underestimate for higher values.

estimates the earlier rates, however the total accumulated rainfall matches quite well. The observed rainfall at Hilo is underestimated: this is probably at least partly due to the relatively low values of PW standard deviations that are calculated for this site but, as in all these cases, may be also due to the inability of PW alone to provide enough information to accurately predict rainfall.

Interestingly, even though the MSM does better at matching the total 24-hour rainfall for low-rainfall sites, in many cases the GPS is better at predicting individual spikes in the rainfall. This is even more obvious for the high-rainfall sites where the MSM persistently underestimates rainfall almost all the time. This does not imply that the GPS is better at predicting rainfall: the algorithm we have developed here is an *a posteriori* model and so it cannot be meaningfully compared with the MSM, however it does indicate that the PW is not being adequately predicted by the MSM. This is illustrated in Figure 4.11 where the MSM predicted PW is plotted against the GPS estimated PW. The MSM is clearly underestimating PW for most of the range, and particularly for higher values. The effect this has on the rainfall predictions is illustrated in Figure 4.12 where the MSM misfits for the precipitable water and the rainfall at the same four GPS/rain gauge site pairs used to generate the GPS rainfall algorithm above are shown. Although the data show broad scatter and one extreme outlier, the linear correlation between the underestimate of PW and the underestimate of rainfall is clear. Encouragingly the best-fit line passes very close to the origin, indicating that where the PW is well modeled the predicted rainfall also matches the observations, suggesting that there is no inherent bias in the MSM predictions.

Conclusions

We use a GPS network over Kīlauea and Mauna Loa volcanoes to image the precipitable water field of the Kaʻū Storm, as it passed over this portion of the island. The subsidence ahead of the system, and rapid increase in PW as the storm impacts the island are clearly visible in the time series. The timing of the main PW peaks across the network along with the rain gauge records suggests that there were two main rain events, while short period spikes illustrate the small-scale variability of the PW field.

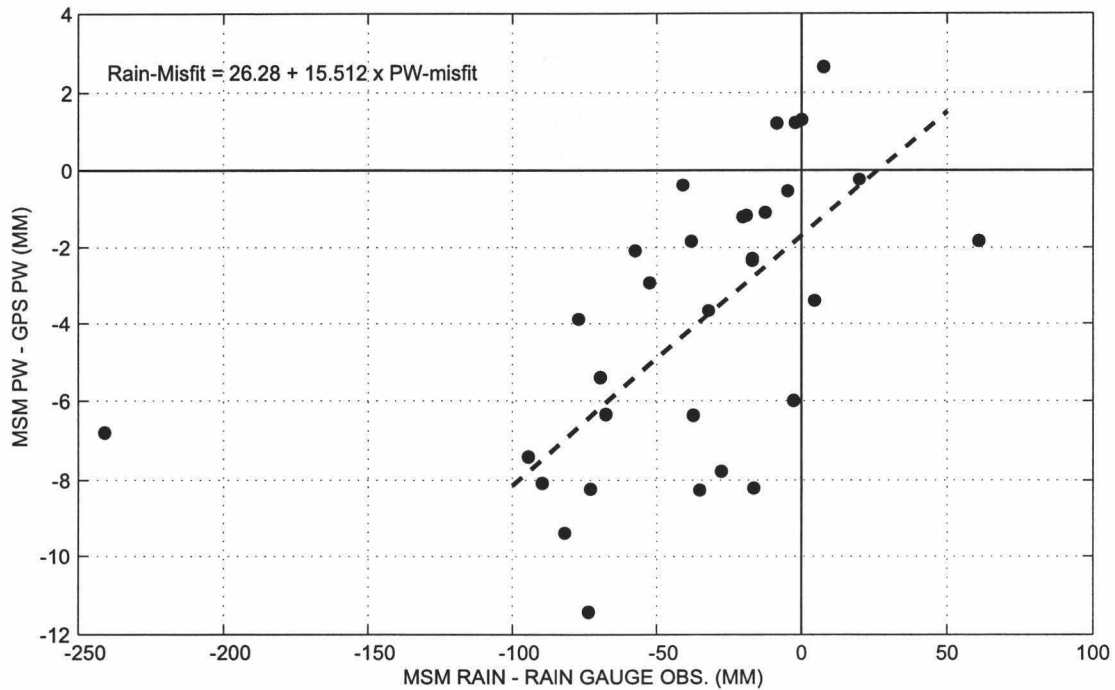


Figure 4.12. Misfit between MSM predicted rainfall and observed rainfall plotted against the misfit between MSM predicted precipitable water and GPS estimated precipitable water. Dashed line indicates median fit to the data with the one extreme outlier removed.

We develop a heuristic normalizing approach for the PW based on climatological statistics that allows us to visualize the relative PW distribution more effectively. Examining these maps of the PW field highlights the spatial structure of the convective system, revealing how the topography of Kīlauea and the south flank of Mauna Loa anchors the storm system leading to prolonged intense convection and rainfall.

Using the observed correlation between the PW and the measured rainfall we construct an algorithm to estimate rainfall from the PW. Overall our algorithm predicts the actual rainfall to within 50% for most sites, although a few sites were much less well modeled. These sites are typically the drier ones, illustrating that the PW alone is insufficient to fully model the precipitation, but suggesting that GPS estimates might serve to provide likely maximum rainfall estimates. The GPS PW correlation with rainfall also suggests that there is a level of excess PW above which rainfall will always occur and which may also provide useful constraints for prediction and interpretation of storm events.

Comparing the GPS derived PW with the rainfall and PW predicted by the MSM predictions we conclude that the shortfall in the MSM rainfall predictions is largely due to its underestimate of PW. Although incorporating GPS PW data into the MSM is likely to be of limited benefit in terms of weather forecasting as it can only provide information on the PW over the islands and not for the critical upstream zone, the fact the PW was underestimated by the MSM for virtually every epoch at every location suggests that the GPS PW could at least help provide better initialization values, leading to some improvement in its performance, particularly in extreme weather.

A more valuable role for GPS in weather forecasting for island locations however would be to provide absolute PW calibrations for satellite maps of the regional PW field. This would combine the accuracy and continuous time coverage of GPS with the broad spatial coverage, but low absolute accuracy PW available from satellites.

Acknowledgements

We thank HVO and Stanford in general and Asta Miklius, Michael Lisowski, Peter Cervelli and Paul Segall in particular for access to the data from their GPS network. The National Park Service Air Resources Division provided some of the surface meteorological data used and the NCEP Reanalysis data was provided by the NOAA-CIRES Climate Diagnostics Center, Boulder, Colorado, from their Web site at <http://www.cdc.noaa.gov/>.

References

- Aitchison, J., and J.A.C. Brown, *The Lognormal Distribution*, University Press, Cambridge, 1957.
- Anthes, R.A., Regional Models of the Atmosphere in Middle Latitudes, *Monthly Weather Review*, 111 (6), 1306-1335, 1983.
- Bevis, M., S. Businger, S. Chiswell, T.A. Herring, R.A. Anthes, C. Rocken, and R.H. Ware, GPS Meteorology: Mapping Zenith Wet Delays onto Precipitable Water, *Journal of Applied Meteorology*, 33, 379-386, 1994.
- Bevis, M., S. Businger, T.A. Herring, C. Rocken, R.A. Anthes, and R.H. Ware, GPS Meteorology: Remote Sensing of Atmospheric Water Vapor using the Global Positioning System, *Journal of Geophysical Research*, 97, 15,787-15,801, 1992.
- Biondini, R., Cloud Motion and Rainfall Statistics, *Journal of Applied Meteorology*, 15 (3), 205-224, 1976.
- Businger, S., S.R. Chiswell, M. Bevis, J. Duan, R.A. Anthes, C. Rocken, R.H. Ware, M. Exner, T. VanHove, and F.S. Solheim, The Promise of GPS in Atmospheric Monitoring, *Bulletin of the American Meteorological Society*, 77 (1), 5-18, 1996.
- Cervelli, P., P. Segall, K. Johnson, M. Lisowski, and A. Miklius, Sudden aseismic fault slip on the south flank of Kilauea Volcano, *Nature*, 415 (6875), 1014-1018, 2002.
- Chen, Y.-L., and J. Feng, Numerical simulations of airflow and cloud distributions over the windward side of the Island of Hawaii. Part I: The effects of trade wind inversion, *Monthly Weather Review*, 129, 1117-1134, 2001.
- Chen, Y.-L., and A.J. Nash, Diurnal variation of surface airflow and rainfall frequencies on the Island of Hawaii, *Monthly Weather Review*, 122, 34-56, 1994.

- Davis, J.L., Atmospheric water-vapor signals in GPS data: synergies, correlations, signals and errors, *Physics and Chemistry of the Earth, Part A: Solid Earth and Geodesy*, 26 (6-8), 513-522, 2001.
- Dick, G., G. Gendt, and C. Reigber, First experience with near real-time water vapor estimation in a German GPS network, *Journal of Atmospheric and Solar-Terrestrial Physics*, 63, 1295-1304, 2001.
- Duan, J., M. Bevis, P. Fang, Y. Bock, S. Chiswell, S. Businger, C. Rocken, F. Solheim, T.v. Hove, R. Ware, S. McClusky, T.A. Herring, and R.W. King, GPS Meteorology: Direct estimation of the absolute value of precipitable water, *Journal of Applied Meteorology*, 35, 830-838, 1996.
- Emardson, T.R., and H.J.P. Derks, On the relationship between the wet delay and the integrated precipitable water vapour in the European atmosphere., *Meteorological Applications*, 7, 61-68, 2000.
- Fang, P., M. Bevis, Y. Bock, S. Gutman, and D. Wolfe, GPS meteorology: Reducing systematic errors in geodetic estimates for zenith delay, *Geophysical Research Letters*, 25, 3583-3586, 1998.
- Fang, P., Y. Bock, and M.v. Domselaar, Hourly updated GPS orbit prediction using sliding window approach, *International Symposium on GPS*, 1999.
- Feng, J., and Y.-L. Chen, Numerical simulations of airflow and cloud distributions over the windward side of the Island of Hawaii. Part II: Nocturnal flow regime, *Monthly Weather Review*, 129, 1135-1147, 2001.
- Foster, J., M. Bevis, and W.H. Raymond, Lognormal distribution of precipitable water in Hawaii, *Geophysical Research Letters*, submitted 2002.
- Giambelluca, T.W., M.A. Nullet, and T.A. Schroeder, Hawaii Rainfall Atlas, pp. 267, Hawaii Division of Water and Land Development, Department of Land and Natural Resources, Honolulu, 1986.

- Gutman, S.I., and S.G. Benjamin, The role of ground-based GPS meteorological observations in numerical weather prediction, *GPS Solutions*, 4, 16-24, 2001.
- Hogg, D.C., F.O. Guiraud, and M.T. Decker, Measurement of excess transmission length on earth-space paths, *Astronomy and Astrophysics*, 304-307, 1981.
- Juvik, S.P., and J.O. Juvik, Atlas of Hawaii, University of Hawai'i Press, Honolulu, 1998.
- King, R.W., and Y. Bock, Documentation for the GAMIT GPS Analysis Software version 10.03, Massachusetts Institute of Technology, Cambridge, 2000.
- Kodama, K., and G.M. Barnes, Heavy Rain Events over the South-Facing Slopes of Hawaii: Attendant Conditions, *Weather and Forecasting*, 12 (2), 347-367, 1997.
- Kodama, K.R., and S. Businger, Weather and Forecasting Challenges in the Pacific Region of the National Weather Service, *Weather and Forecasting*, 13 (3), 523-546, 1998.
- Lawson, C.L., and R.J. Hanson, *Solving Least Squares Problems*, Prentice Hall, Englewood Cliffs, New Jersey, 1974.
- Lichten, S.M., and J.S. Border, Strategies for high precision Global Positioning System orbit determination, *Journal of Geophysical Research*, 92, 12,751-12,762, 1987.
- López, R.E., The Lognormal Distribution and Cumulus Cloud Populations, *Monthly Weather Review*, 105 (7), 865-872, 1977.
- Motell, C., J. Porter, J. Foster, M. Bevis, and S. Businger, Comparison of precipitable water over Hawaii using AVHRR-based split-window techniques, GPS and radiosondes, *International Journal of Remote Sensing*, 23 (No. 11), 2335-2339, 2002.
- Neill, A.E., Global mapping functions for the atmosphere delay at radio wavelengths, *Journal of Geophysical Research*, 101, 3227-3246, 1996.
- O'Neill, N.T., A. Ignatov, B.N. Holben, and T.F. Eck, The lognormal distribution as a reference for reporting aerosol optical depth statistics; Empirical tests using multi-year, multi-site AERONET sunphotometer data, *Geophys. Res. Lett.*, 27 (20), 3333-3336, 2000.
- Raymond, W.H., Moisture Advection Using Relative Humidity, *Journal of Applied Meteorology*, 39 (12), 2397-2408, 2000.

- Ross, R.J., and S. Rosenfeld, Estimating mean weighted temperature of the atmosphere for Global Positioning System applications, *Journal of Geophysical Research*, 102, 21,719-21,730, 1997.
- Ross, R.J., and S. Rosenfeld, Correction to "Estimating mean weighted temperature of the atmosphere for Global Positioning System applications", *Journal of Geophysical Research*, 104, 27,625, 1999.
- Saastamoinen, J., *Atmospheric correction for the troposphere and stratosphere in radio ranging of satellites*, AGU, 1972.
- Schroeder, T.A., Mesoscale Structure of Hawaiian Rainstorms, pp. 69pp, Water Resources Research Center, Honolulu, 1978.
- Starr, D.O.C., and S.H. Melfi, The Role of Water Vapor in Climate, in *NASA Conference Publication*, pp. 50, 1991.
- Tregoning, P., R. Boers, D. O'Brien, and M. Hendy, Accuracy of absolute precipitable water vapor estimates from GPS observations, *Journal of Geophysical Research*, 103, 28,701-28,710, 1998.
- Treuhaft, R.N., and G.E. Lanyi, The effect of the dynamic wet troposphere on radio interferometric measurements, *Radio Science*, 22, 251-265, 1987.
- Tralli, D.M., T.H. Dixon, and S.A. Stephens, Effect of wet tropospheric path delays on estimation of geodetic baselines in the Gulf of California using the Global Positioning System, *Journal of Geophysical Research*, 93, 6545-6557, 1988.
- Wang, B., R. Wu, and X. Fu, Pacific-East Asian Teleconnection: How Does ENSO Affect East Asian Climate?, *Journal of Climate*, 13 (9), 1517-1536, 2000.
- Wang, J.-J., H.-M.H. Juang, K. Kodama, S. Businger, Y.-L. Chen, and J. Partain, Application of the NCEP Regional Spectral Model to Improve Mesoscale Weather Forecasts in Hawaii, *Weather and Forecasting*, 13 (3), 560-575, 1998.

- Williams, S., Y. Bock, and P. Fang, Integrated satellite interferometry: Tropospheric noise, GPS estimates and implications for interferometric synthetic aperture radar products, *Journal of Geophysical Research*, 27,051-27,067, 1998.
- Wolfe, D.E., and S.I. Gutman, Developing an Operational, Surface-Based, GPS, Water Vapor Observing System for NOAA: Network Design and Results, *Journal of Atmospheric and Oceanic Technology*, 17 (4), 426-440, 2000.
- Zhang, Y.-X., Y.-L. Chen, H.-M.H. Juang, S.-Y. Hong, K. Kodama, and R. Farrell, Validation and sensitivity tests of the mesoscale spectral model simulations over the Hawaiian islands, *2nd Regional Spectral Model Workshop, MHPCC, Maui, Hawaii*, 2000.